The Astrophysical Journal, 645:17–43, 2006 July 1

OBSERVATION OF SMALL-SCALE STRUCTURE USING SEXTUPOLE LENSING

John Irwin and Marina Shmakova
Stanford Linear Accelerator Center, Stanford University, P.O. Box 4349, CA 94309; irwin@slac.stanford.edu, shmakova@slac.stanford.edu
Received 2003 September 10; accepted 2006 February 24

ABSTRACT

Gravitational lensing by foreground halos with masses as small as $10^{10}\,M_{\odot}$ can induce observable second-order shape distortions in background galaxy images in addition to the well-known elliptical shape distortion produced by first-order shear. Furthermore, the orientation of the second-order distortions is correlated with the orientation of the shear-induced elliptical (quadrupolar) shape. Because of its angular dependence, we refer to the most prominent second-order distortion as a sextupole distortion. The correlation between first-order and second-order shapes provides a sensitive signal by which to identify galaxies that may have been lensed. Galaxy images appear to be slightly curved by these lensing events. In this paper we develop a general theoretical lensing framework based on a lensing distortion map. Tools to infer map coefficients from the galaxy images are described and applied to the Hubble Deep Field–North. Instrumental PSFs, camera charge diffusion, and image composition methods are modeled in the coefficient determination process. Estimates of Poisson counting noise for each galaxy are used to cut galaxies with signals too small to reliably establish curvature. These noise estimates are confirmed using a Fisher matrix analysis. Background shape distortions may also be represented by maps. Curved galaxies are found to be spatially clumped, as might arise from sextupole lensing by overdensities in a foreground dark matter halo distribution. We calculate the cross section for sextupole lensing by Moore and NFW halos and estimate the total cross section of the field based on these halo cross sections.

Subject headings: dark matter — galaxies: clusters: general — gravitational lensing

Online material: color figures

1. INTRODUCTION

Weak gravitational lensing methods (for review, see Bartelmann & Schneider 2001; Mellier 1999; Hoekstra et al. 2002a; and recently Schneider 2006) allow one to investigate the evolution of matter clustering and the growth of large-scale structure (Wittman et al. 2000; Mellier et al. 2002) and thus probe the properties of both dark energy and dark matter. It is a unique way to investigate both the past and future of the universe. Structure growth is understood as the growth of the matter density fluctuations predicted by inflationary cosmology and dark energy evolution (for review, see Peebles 1993), and hence the structure of density fluctuations provides information about inflationary scenarios (Huterer & Turner 2001; Huterer 2002; Linder & Jenkins 2003). On the other hand, the matter distribution measurements give bounds on the dark energy equation of state, allowing one to predict the future of the universe (Linde 2004; Kallosh & Linde 2003; Kallosh et al. 2003).

1.1. *The Sextupole Lensing Method*

In this paper we present a new method of lensing that we call "sextupole lensing." Sextupole lensing derives its name from the fact that when the distance between the lensing mass and the lensed background galaxy light path is small (say, $\sim$10 kpc), a distinctive second-order moment having three maxima and three minima, called a sextupole moment, can be induced in the background galaxy image. This moment is superimposed on a quadrupole moment (also called ellipticity, having two maxima and two minima) produced by the linear lensing deflection known as shear. Surprisingly, sextupole lensing can probe mass scales as small as $10^{9}\,M_{\odot}$, because the second-order deflection inducing the sextupole moment varies in strength as $1/R^3$ and hence can be large when the impact parameter R is small. Thus, sextupole lensing can probe structure on small scales.

A crucial feature of the induced sextupole moment is that its orientation is correlated with the orientation of the induced quadrupole moment; one of the minima of the sextupole moment will be aligned with one of the minima of the quadrupole moment, giving the image a slightly curved appearance. The familiar curving seen in strong-lensing arclets (Bartelmann & Schneider 2001; Mellier 1999) can be understood as the correlated superposition of quadrupole and sextupole moments, with the length of the arclet usually being determined by the local strength of a yet higher order octupole moment. Curved features might also be apparent in galaxy-galaxy lensing (Brainerd et al. 1996; Hoekstra et al. 2002b; Natarajan & Refregier 2000; Hoekstra 2004).

The typical cluster identifiable through weak lensing (Kaiser et al. 2000) has a mass of $10^{14}\,M_{\odot}$ and a radius of about 500 kpc. Since the strength of the quadrupole deflection, responsible for the ellipticity, is proportional to the mass and falls off like $1/R^2$, one could get the same induced quadrupole moment in a light stream positioned 5 kpc from an object of $10^{10}\,M_{\odot}$. In the latter example, since the sextupole moment varies as $1/R^3$, the sextupole moment becomes 100 times stronger, becoming as large as the intrinsic sextupole moments of the background galaxies. If ensembles of dark matter contain an abundance of lower mass clumps, the light streams passing through them might occasionally pass close to a 10^{9}–$10^{13}\,M_{\odot}$ object, producing an observable sextupole moment in the image (Irwin & Shmakova 2004).

Since this "close-encounter" lensing creates an alignment of the minima of quadrupole and sextupole moments in the lensed background galaxies, a foreground population of objects with high-density interiors would be detectable through the background galaxies as a spatial correlation in this particular orientation of sextupole moments with respect to quadrupole moments (a spatial correlation of an angular correlation). To see this correlation signal, one would first identify background galaxies whose sextupole and quadrupole moments are aligned as if they could have arisen

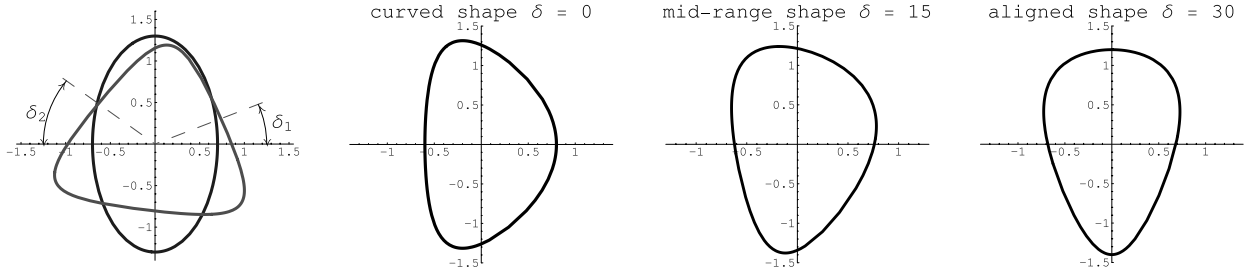

FIG. 1.—Arbitrarily oriented quadrupole and sextupole shape distortions (*left*). The minimum angle between a quadrupole minimum and a sextupole minimum is denoted by $\delta = \delta_1$ if $|\delta_1| < 30^\circ$; otherwise, $\delta = \delta_2$. We are then guaranteed that $-30^\circ \leq \delta \leq 30^\circ$. Curved galaxies are defined as those for which $|\delta| \leq 10^\circ$, midrange galaxies by $10^\circ < |\delta| < 20^\circ$, and aligned galaxies by $|\delta| \geq 20^\circ$. [*See the electronic edition of the Journal for a color version of this figure*.]

from lensing, and then one would look to see whether such galaxies are located on the sky randomly, or whether, on the other hand, they were clumped. This is the program that we develop in this paper and then apply to the Hubble Deep Field–North (HDF-N).[1]

In addition, if the background light stream penetrates a mass clump at a location where the mass density gradient is nonzero, two other second-order moments (with a rotational dependence of the dipole moment) can be induced. The orientation of those moments is correlated with both the quadrupole and sextupole moments.

1.2. *Sextupole Lensing From a Point Mass*

We begin with the simple case of a concentrated point mass. The $1/R$ gravitational deflection (which we sometimes refer to as an impulse or kick, because the details of the deflection along the trajectory of the centroid can be integrated out) of a light stream can be expanded in a power series. With a dark matter clump at the origin, and the beam centroid at position x_0, the deflection $\Delta x'$ of a ray at the coordinate position $X = x_0 + x$ is given as

$$\Delta x' = -\frac{4MG}{X} = -\frac{4MG}{x_0 + x} = -\frac{4MG}{x_0}\left[1 - \frac{x}{x_0} + \left(\frac{x}{x_0}\right)^2 + \ldots\right], \tag{1}$$

where x indicates the offset from the centroid within the light stream. Each term in the power series is down from the previous term by the fraction x/x_0. In order for the effects of higher order terms to be seen, the impact parameter x_0 must be only a small multiple of the light-stream width.

This power series expansion can be generalized to yield the deflection in both coordinates. The deflection, when including the direction, in cylindrical coordinates is proportional to $-e^{i\Theta}/R = -1/(e^{-i\Theta}R) = 1/(X - iY)$. Setting $X = x_0 + x$ and $Y = y$, we obtain

$$\Delta x' + i\Delta y' = -\frac{4MG}{(X - iY)} = -\frac{4MG}{x_0 + (x - iy)} = -\frac{4MG}{x_0}\left[1 - \frac{x - iy}{x_0} + \left(\frac{x - iy}{x_0}\right)^2 + \ldots\right]. \tag{2}$$

Expressions for general mass distributions are provided in § 2. Concentrating first on the linear term, one sees that the horizontal kick is defocusing, while the vertical kick is focusing. The image appears larger in the focused direction and smaller in the defocused direction, and hence the linear term changes a circle into an ellipse. It is a general feature that the image distortions have the opposite sign of the deflections: for example, a deflection to the left results in the observed image moving to the right.

Introducing polar coordinates (r, θ) for the coordinates (x, y) yields

$$\Delta x' + i\Delta y' = -\frac{4MG}{x_0}\left[1 - \frac{r}{x_0}e^{-i\theta} + \left(\frac{r}{x_0}\right)^2 e^{-i2\theta} + \ldots\right]. \tag{3}$$

The leading constant deflection term in equation (3) is called the dipole term: all rays in the light stream receive the same deflection. In beam physics the dipole term is created by a magnet having two poles, and the radial distortion has one maximum and one minimum. The first-order (linear) term is called the quadrupole term, since it is the deflection created by a magnet with four poles, and because the distortions of a radially symmetric beam, when viewed downstream, would be elliptical (i.e., quadrupolar) in form. The notation "quadrupole" also reflects a 2θ modulation of the radial shape, having two maxima and two minima.[2] The second-order term is called a "sextupole," because it is the deflection given by a magnet with six poles and results in an image distortion with a 3θ behavior having three maxima and three minima. The quadrupole and sextupole shapes are sketched in the left panel of Figure 1.

For a point mass at the origin and a light stream on the x-axis, as above, a ray farther out the x-axis (for which $\theta = 0$) will have a negative first-order deflection and a positive second-order deflection. There, the quadrupole distortion has a minimum and the sextupole distortion has a maximum. At $\theta = \pi$ the quadrupole has its other minimum, but here the sextupole has a minimum. The middle and right panels of Figure 1 show the superposition of quadrupole and sextupole distortions for two distinct orientations of the sextupole. The second panel corresponds to the curved shape that would arise from a lensing event with minima aligned. In the rightmost panel, we see the shape that results when quadrupole and sextupole maxima are aligned. Such a shape would not be created from a single lensing event with a radially symmetric mass distribution.

The plan we follow in this paper is to measure the quadrupole and sextupole shape of all background galaxies and classify each galaxy according to whether it is "curved," "midrange," or "aligned," as defined by the criteria described in Figure 1. We then examine the distribution of curved galaxies on the sky to

[1] See http://www.stsci.edu/ftp/science/hdf/hdf.html.

[2] At position $re^{i\theta}$ the deflection direction of the first-order term is $e^{-i\theta}$, which is at an angle 2θ from the radial direction. Therefore, at constant radius r the radial distortion will be proportional to $\cos 2\theta$.

determine whether such galaxies are randomly distributed or unusually clumped.

Our central conceptual tool, the lensing distortion map, is introduced in § 2. The coefficients appearing in the map are each described and compared with common lensing terminology. Expressions for the coefficients from lensing by azimuthally symmetric distributions are derived and applied to lensing from NFW (Navarro-Frenk-White; Navarro et al. 1995, 1996, 1997) and Moore (Moore 1994; Moore et al. 1998, 1999) distributions.

Section 3 describes three increasingly sophisticated methods for inferring the coefficients of the map for each background galaxy. The first method, the moment method, is based on image moments. The second method, the radial-fit method, uses the best fit of a mapped (initially symmetric) galaxy shape parameterized in a simple form. The third method, the model method, expands on the second method to include effects of the point-spread function, charge diffusion in the camera, and important features of the image composition process.

Section 4 describes the selection and general properties of galaxies in the Hubble Deep Fields. Section 5 presents the results of each of the three methods for determination of the quadrupole coefficient. An analytical estimate for the noise in the quadrupole coefficient, based on Poisson noise of the galaxy image, is presented, and noise cuts are implemented. Section 6 presents the results of each of the three methods for determination of the sextupole coefficient. We complete the measurement section by presenting the distributions found for the principal parameter of interest to us, the angle between quadrupole minimum and sextupole minimum, by which we distinguish the three shape categories labeled "curved," "midrange," and "aligned."

The primary goal of the above development is presented in § 7. There we describe and employ a nearest neighbors analysis to quantify clumping. Then we determine the probability of obtaining the observed clumping randomly, keeping galaxy locations fixed in the sky while permuting their properties. Both the curved and aligned galaxy subsets are determined to be more clumped than randomly chosen subsets at the 2 σ level.

Section 8 addresses possible systematic sources of clumping, such as correlated curvature originating among the background galaxies themselves or correlated curvature from an uncompensated residual of the point-spread function.

In § 9 we examine the consistency of our clumping result with suspected features of the ΛCDM concordance model. In particular, we make a first-order estimate as to whether lensing by overdensities among the dark matter foreground galaxies could account for this result. Section 10 summarizes the paper.

2. LENSING DISTORTION MAPS

2.1. *Setting up the Map*

In the standard lensing situation, rays from a distant background galaxy are deflected by a mass concentration. The apparent image, as seen from the position of the telescope, is defined by an intensity function that depends only on the angle of each ray as it enters the telescope. Going backward, toward the apparent image, the rays are deflected by mass distributions but are known to depart somewhere from the source galaxy. The ray will have a definite position and angle at the source galaxy. This backward mapping, which we refer to as the "lensing distortion map," connects coordinate variables (ray position and direction) located at the telescope to coordinate variables (ray position and direction) at the source galaxy. We begin by setting up coordinate systems for these variables with one axis coincident with a light ray from the approximate centroid of the galaxy to the telescope. This ray defines what we call the longitudinal axis, and distance along this axis is designated by the letter s.[3] A position perpendicular to the centroid ray is designated by $(\tilde{x}_S, \tilde{y}_S)$ at the source and $(\tilde{x}_T, \tilde{y}_T)$ at the telescope. We take these variables to be comoving distances.[4]

Using the longitudinal distance s, rather than the time t, as the independent variable, the conjugate momenta are $(\tilde{x}'_S, \tilde{y}'_S)$ (where, e.g., $\tilde{x}'_S = d\tilde{x}_S/ds$ is the slope of the ray). Likewise, $(\tilde{x}'_T, \tilde{y}'_T)$ denotes the momentum vector of the ray at the telescope.

The map of ray locations constructed between telescope and source will be symplectic, since the light geodesics are described by a Hamiltonian, and consequently the determinant of the linear four-dimensional transformation matrix expanded about any ray will equal unity. However, the spatial trajectories of all rays converge to the same point, the position of the telescope, which we take to be $\tilde{x}_T = \tilde{y}_T = 0$. Hence, the two angles $\tilde{x}'_T$ and $\tilde{y}'_T$ at the telescope uniquely describe the ray trajectory through space and its coordinates at the galaxy. Thus, the "backward" map can be written as a set of four functions $\tilde{x}_S(\tilde{x}'_T, \tilde{y}'_T)$, $\tilde{y}_S(\tilde{x}'_T, \tilde{y}'_T)$, $\tilde{x}'_S(\tilde{x}'_T, \tilde{y}'_T)$, and $\tilde{y}'_S(\tilde{x}'_T, \tilde{y}'_T)$.

In the absence of any lensing other than the direction changes suffered by the centroid ray, the angle of a ray from $(\tilde{x}_S, \tilde{y}_S)$ would enter the telescope at the angles $(x'_S, y'_S) = (\tilde{x}_S/D_{TS}, \tilde{y}_S/D_{TS})$, where D_{TS} is the comoving distance from the telescope to the source.[5] Making this identification, the backward map can be represented by the functions $x'_S(x'_T, y'_T)$ and $y'_S(x'_T, y'_T)$, where we have also identified $x'_T \equiv \tilde{x}'_T$ and $y'_T \equiv \tilde{y}'_T$. If desired, these angular coordinates at the telescope entrance can be transformed to an "ideal" position on the focal plane by multiplying by the number of pixels per radian at the galaxy position. The lensing distortion map is then given by functions $x_S(x_T, y_T)$ and $y_S(x_T, y_T)$, where all coordinates are now positions on the ideal focal plane.

The resulting lensing distortion map functions so defined contain the information on what happened in the transit of light rays from the telescope to the source galaxy. To account for distortions present in the transformation from incoming angle to focal plane would require the introduction of an additional map representing them. The map from source to "real" focal plane would then be a concatenation of these two maps.

In this two-dimensional map we have ignored the slopes $\tilde{x}'_S$ and $\tilde{y}'_S$ at the source plane, and hence the two-dimensional determinant is not guaranteed to be unity. Under some circumstances, two distinct rays of the same source galaxy, entering the telescope at slightly different angles, can depart from the same location within a single galaxy, of course having different slopes there. By excluding such situations, there is no loss in dropping the functions $\tilde{x}'_S$ and $\tilde{y}'_S$. This condition is equivalent to demanding that nowhere over the full extent of the image does the Jacobian pass through zero, namely,

$$J(x_T, y_T) = \begin{vmatrix} \dfrac{\partial x_S}{\partial x_T} & \dfrac{\partial x_S}{\partial y_T} \\ \dfrac{\partial y_S}{\partial x_T} & \dfrac{\partial y_S}{\partial y_T} \end{vmatrix} \neq 0. \tag{4}$$

When second-order terms are present in the map, the Jacobian is a quadratic function of position.

[3] We do not rule out the possibility that there could be multiple images from a single galaxy and that there may be more than one such ray. In such a case one independently sets up coordinate systems for each image.

[4] We include tildes here because later we define related coordinates without tildes.

[5] We warn the reader that x'_S and y'_S are not the slopes of an actual ray. They are linear functions of the position. They would equal the actual slopes, $\tilde{x}'_S$ and $\tilde{y}'_S$, only in the absence of lensing.

2.2. *The Map in Complex Coordinates*

The two functions $x'_S(x'_T, y'_T)$ and $y'_S(x'_T, y'_T)$ can be combined into one complex function by defining $w'_S = x'_S + iy'_S$. This complex function can be written in terms of the variables $w'_T = x'_T + iy'_T$ and $\bar{w}'_T = x'_T - iy'_T$ by substituting $x'_T = \frac{1}{2}(w'_T + \bar{w}'_T)$ and $y'_T = (1/2i)(w'_T - \bar{w}'_T)$. The map equations can then be written as the single function $w'_S(w'_T, \bar{w}'_T)$.

Since the transverse width of the light stream will usually be small compared to characteristic dimensions of the variation of the lensing mass distributions, we can expand this function in a power series about the stream centroid,[6]

$$w'_S(w'_T, \bar{w}'_T) = w'_T + \sum_{n,m=0}^{\infty} a_{nm} w'^n_T \bar{w}'^m_T. \quad (5)$$

By introducing the conversion factor to the focal plane α, the number of radians per pixel, the map becomes

$$w_S(w_T, \bar{w}_T) = w_T + \sum_{n,m=0}^{\infty} a_{nm} \alpha^{n+m-1} w^n_T \bar{w}^m_T. \quad (6)$$

The significance of the complex variables w and $\bar{w}$ (or w' and $\bar{w}'$) rests primarily with the fact that products and powers of them are rotation eigenfunctions. It follows that the terms in the expansion for w_S have a simple interpretation.

The coefficients a_{nm} are usually complex, as can be seen by rotating the coordinate system. If one rotates the coordinate system counterclockwise (in the positive θ direction) by the angle ϕ, then w_S and w_T change by $e^{-i\phi}$, and thus a_{nm} must vary as $e^{i(n-1)\phi} e^{-im\phi}$.

The leading term is chosen to be w_T, so that in the case of no lensing whatsoever, all a_{nm} will be zero. This leading term is called the identity map. In addition, one usually sets $a_{00} = 0$, because it would simply shift the origin of the S-variables by a constant, representing the presence of a uniform deflection.

The a_{10} term is invariant under rotations. For lensing by mass on a single plane, we show that the term a_{10} is real, so $1 + a_{10}$ produces a simple scaling. The a_{10} term is often called convergence and denoted by $-\kappa$. However, for lensing maps with lensing at two planes, a_{10} will generally be complex. In that case, the combination $1 + a_{10}$ produces a rotation as well as a scaling. For a single lensing plane it is shown that all a_{nm} with $n > 0$ are zero unless the light-stream centroid actually passes through regions where the lensing mass density or its derivatives are nonzero. The a_{0m} terms can be nonzero even when the light stream passes through empty space.

A general linear two-dimensional transformation, as represented by a 2×2 matrix, has four coefficients. In the complex linear map two real coefficients are contained in a_{10}, and the other two are in a_{01}. According to the argument above, a_{01} varies as $e^{i2\phi}$ under rotations and is the coefficient of $\bar{w}_T = r_T e^{-i\theta_T}$. As described in the discussion of point mass lensing in § 1.2, such a term produces a quadrupolar distortion. When arising from lensing, a_{01} is normally called shear and denoted by the variable $-\gamma$.

The a_{02} term is the coefficient of the second-order term $\bar{w}^2_T$. In polar notation, $\bar{w}^2_T = r^2_T e^{-i2\theta_T}$, which was shown in § 1.2 to produce a sextupolar distortion, having three maxima and three minima.

The a_{11} and a_{20} terms are also second-order coefficients. The a_{11} term is the coefficient of $w_T \bar{w}_T = r^2_T$, which does not depend on angle. Thus, for a circle at constant r_T this term produces a translation whose magnitude increases as r^2_T. The a_{20} term can be shown to produce a cardioid shape.[7] As we show below, for lensing by mass on a single plane, $a_{11} = 2\bar{a}_{20}$. Both terms are zero unless the light-stream centroid passes through the mass distribution.

The third-order term a_{03} yields an octupolar distortion. There are three other third-order terms: a_{12}, a_{21}, and a_{30}. Third-order terms are not discussed further in this paper. They are normally smaller than the sextupole terms, and a spurious octupole can be created by pixelation effects and by the point-spread function.

For the map in terms of the variables w'_T, the second-order coefficient has the units radian^{-1}. Conversion to arcsec^{-1} requires the second-order coefficients to be multiplied by the number of radians per arcsecond, 4.9×10^{-6}. Conversion to the focal plane map specified in terms of pixels requires the second-order coefficients to be further multiplied by the number of arcseconds per pixel, which equals 0.04 for the drizzled HDF images. We have chosen to use the focal plane representation of the map, because the images are presented and processed in pixel units. In addition, since the majority of our images are only a few pixels in radius, one can compare the sextupole strength at the rms radius with the quadrupole strength by multiplying the sextupole coefficient by the rms radius in pixels.

2.3. *The Map from a Single Lensing Plane*

We now turn to maps arising from mass distributions that can adequately be represented by mass projected onto a single plane (which we refer to as the lensing plane). To determine the Green's function for this case, consider the effect of a point mass. A light stream passing at distance r will be deflected radially by the angle $\Delta r' = -4MG/r$. The potential for such a kick, the sought Green's function, is $2\Phi_\delta = 4MG \ln(r)$. However, this is just the Green's function for the two-dimensional Laplace equation, $\nabla^2 \Phi = 4\pi G\Sigma$, where Σ is the surface mass density function.[8]

In accord with the variables chosen for the map, we expand the solution to Laplace's equation in the variables $w = x + iy$ and $\bar{w} = x - iy$. (Variables without subscripts T or S are taken to lie in the lensing plane.) To enable power series expansions, it is useful to introduce derivative operators $\partial \equiv \partial/\partial w \equiv \frac{1}{2}[\partial/\partial x - i(\partial/\partial y)]$ and $\bar{\partial} \equiv \partial/\partial \bar{w} \equiv \frac{1}{2}[\partial/\partial x + i(\partial/\partial y)]$, which have the desired property that $\partial w = \bar{\partial}\bar{w} = 1$ and $\partial \bar{w} = \bar{\partial} w = 0$.

Using these variables, the power series expansion for the potential is $\Phi(w, \bar{w}) = \sum_{n,m=0}^{\infty} (1/n!m!) \Phi_{nm} w^n \bar{w}^m$, where $\Phi_{nm} = \partial^n \bar{\partial}^m \Phi$ evaluated at $w = w_0$. The reality condition on Φ implies relationships among these coefficients. For example, the Φ_{nn} are real and $\Phi_{nm} = \overline{\Phi_{mn}}$. If both $n > 0$ and $m > 0$, the term will be proportional to the density or a derivative of the density, since $\Phi_{11} = \frac{1}{4}\nabla^2 \Phi = \pi G\Sigma$. The two components of the kick, given in the form $\Delta x' + i\Delta y'$, are contained in the single equation

$$\Delta w' = -2\bar{\partial}(2\Phi) = -4 \sum_{n,m=0}^{\infty} \frac{1}{n!m!} \Phi_{nm+1} w^n \bar{w}^m. \quad (7)$$

Here we took a derivative of the power series expression for Φ and then set $m \to m + 1$ in the sum.

The geometry of Figure 2 implies

$$w'_S = w'_T + \frac{D_{LS}}{D_{TS}} \Delta w'(w, \bar{w}), \quad (8)$$

[6] This condition is violated in the case of arcs.

[7] Subsequent to the original posting of this paper, other authors suggested the name second flexion for the sextupole term and the name first flexion for the terms a_{11} and a_{20} (Goldberg & Bacon 2005; Bacon et al. 2006).

[8] Here Φ is the potential for the deflection of a nonrelativistic particle. The factor of 2 is explicitly retained, indicating that light rays receive twice this kick.

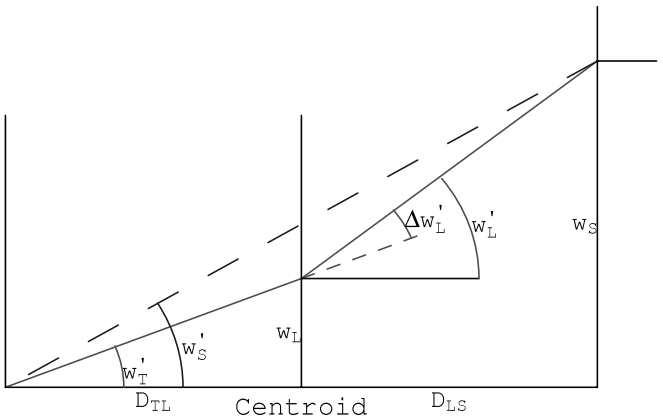

FIG. 2.—Symbolic diagram showing the lensing geometry for a single ray assuming a single lensing plane. The diagram follows the centroid, which is identified with the horizontal axis. All distances (D_{TL}, between telescope and lensing plane; D_{LS}, between lensing plane and source; w_L, from the centroid to the ray at the lensing plane; and w_S, from the centroid to the ray at the source plane) are to be understood as comoving distances. To calculate the angle $\Delta w'_L$, the position of the ray when passing the plane [namely, $w = w_L/(1 + z_L)$] must be used in the deflection formula. The geometry for a map in the case of multiple lensing planes may be set up in this same way. This diagram provides the relationships $w_L = D_{TL}w'_T$ and $w_S = D_{TS}w'_T + D_{LS}\Delta w'_L$, where $D_{TS} = D_{TL} + D_{LS}$. A flat universe is assumed throughout. [*See the electronic edition of the Journal for a color version of this figure.*]

where

$$w = \frac{D_{TL}}{1 + z_L} w'_T.$$

The factors here can be understood as follows. First, multiply through by the comoving distance to the source plane, D_{TS}. Then the left-hand side is the comoving location of the ray on the source plane. This is given as a function of the initial angle of the ray leaving the telescope, w'_T. The first term on the right-hand side is the comoving position on the source plane of the unperturbed ray departing at angle w'_T. The second term is the modification in that ray's position on the source plane as a result of a kick that occurs at a distance D_{LS} preceding the source plane. The kick is given by equation (7), where w is understood to be the distance from the centroid in that plane at the moment in time when the light stream passed, namely, the comoving location, $D_{TL}w'_T$ divided by $1 + z_L$. This reasoning may be easily extended to yield the map for lensing on two planes.

From equation (8) we can derive the map coefficients for a general potential,

$$\begin{aligned}
a_{10} &= -4\frac{D_{LS}}{D_{TS}}\frac{D_{TL}}{1+z_L}\Phi_{11} = -4\pi G\frac{D_{LS}}{D_{TS}}\frac{D_{TL}}{1+z_L}\Sigma(r_0),\\
a_{01} &= -4\frac{D_{LS}}{D_{TS}}\frac{D_{TL}}{1+z_L}\Phi_{02},\\
a_{02} &= -4\frac{D_{LS}}{D_{TS}}\left(\frac{D_{TL}}{1+z_L}\right)^2\frac{1}{2}\Phi_{03},\\
a_{11} &= -4\frac{D_{LS}}{D_{TS}}\left(\frac{D_{TL}}{1+z_L}\right)^2\Phi_{12}\\
&= -2\pi G e^{i\theta_0}\frac{D_{LS}}{D_{TS}}\left(\frac{D_{TL}}{1+z_L}\right)^2\frac{\partial\Sigma}{\partial r}(r_0),\\
a_{20} &= -4\frac{D_{LS}}{D_{TS}}\left(\frac{D_{TL}}{1+z_L}\right)^2\frac{1}{2}\Phi_{21}\\
&= -\pi G e^{-i\theta_0}\frac{D_{LS}}{D_{TS}}\left(\frac{D_{TL}}{1+z_L}\right)^2\frac{\partial\Sigma}{\partial r}(r_0).
\end{aligned} \tag{9}$$

The coordinates (r_0, θ_0) are the location of the light-stream centroid in the frame of reference on which the lensing mass distribution is described. The term r_0 is the distance of separation at the epoch when the light stream passed the plane.

The map coefficients for a point source can be found by evaluating the derivatives of $2\Phi_\delta = 4MG\ln(r) = 2MG\ln(w\bar{w})$,

$$\begin{aligned}
a_{01\delta} &= \frac{D_{LS}}{D_{TS}}\frac{D_{TL}}{1+z_L}\frac{4MG}{\bar{w}_0^2},\\
a_{02\delta} &= -\frac{D_{LS}}{D_{TS}}\left(\frac{D_{TL}}{1+z_L}\right)^2\frac{4MG}{\bar{w}_0^3},\\
a_{10\delta} &= a_{11\delta} = a_{20\delta} = 0.
\end{aligned} \tag{10}$$

The map coefficients can be found for any symmetric mass distribution by using Gauss's law, $\partial\Phi/\partial r = 2M(r)G/r = (4\pi G/r)\int_0^r \Sigma(r')r'\,dr'$, and the relationship $\bar{\partial}\Phi(r) = (w/2r)[\partial\Phi(r)/\partial r]$. Using these relationships, one finds

$$\begin{aligned}
a_{01} &= 4Ge^{i2\theta_0}\frac{D_{LS}}{D_{TS}}\frac{D_{TL}}{1+z_L}\left[\frac{M(r_0)}{r_0^2} - \pi\Sigma(r_0)\right],\\
a_{02} &= -4Ge^{i3\theta_0}\frac{D_{LS}}{D_{TS}}\left(\frac{D_{TL}}{1+z_L}\right)^2\left[\frac{M(r_0)}{r_0^3} - \frac{\pi\Sigma(r_0)}{r_0} + \frac{\pi\Sigma'(r_0)}{4}\right].
\end{aligned} \tag{11}$$

We note that the magnitude of the Σ term in the expression for a_{01}, including coefficients, is the same as the expression for a_{10} in equation (9). In addition, the magnitude of the first two terms in the equation for a_{02} is precisely $D_{TL}/[(1 + z_L)r_0]$ times the equation for a_{01}. Since a_{02} gets multiplied by an extra $\bar{w}'_0$, the ratio of magnitudes is just the light-stream size at epoch z_L divided by the distance to the center, reflecting the simple relationship in equation (1).

For the remainder of this paper we use the notation $a = a_{01}$ for the quadrupole coefficient and $b = a_{02}$ for the sextupole coefficient. Since they are the coefficients of distinct shapes, we set $d_1 = a_{11}$ and $d_2 = a_{20}$. In the case of lensing from a single plane, the lensing-induced coefficients would have the relationship $d_1 = 2d_2$. When we impose this condition, we use the notation $d = d_2 = d_1/2$.

We purposely avoid the use of the words "convergence" or the symbol $-\kappa$ for a_{10} and "shear" or the symbol $-\gamma$ for a_{01}, because convergence and shear are usually meant to indicate a physical property of the galaxy field. While it is our intention to extract such physical information using maps, it will become evident (see, e.g., § 3.4) that there are many maps to consider whose quadrupole coefficients do not represent shear. However, quadrupole terms are always quadrupole terms.

Figure 3 shows a log-log plot of the scaled mass profile and the coefficient strengths in the case of an NFW and Moore halo profile. We discuss these results further in § 9. For now, we note that the coefficients depend strongly on details of the halo profile. For example, if the density profile was a constant plus a polynomial in r^2 near the origin, the quadrupole coefficient would go to zero as $\sim r^2$ at the origin, and the sextupole coefficient would go to zero as $\sim r^3$. Density profiles with singularities behave quite differently.

The top panels of Figure 4 provide a sense of the shapes arising from the different individual terms in the map. The bottom panels show the appearance of typical combinations.

3. EXTRACTION OF MAP COEFFICIENTS FROM IMAGES

We use three distinct methods to estimate lensing map coefficients: (1) a moment method, (2) a radial-fit method, and

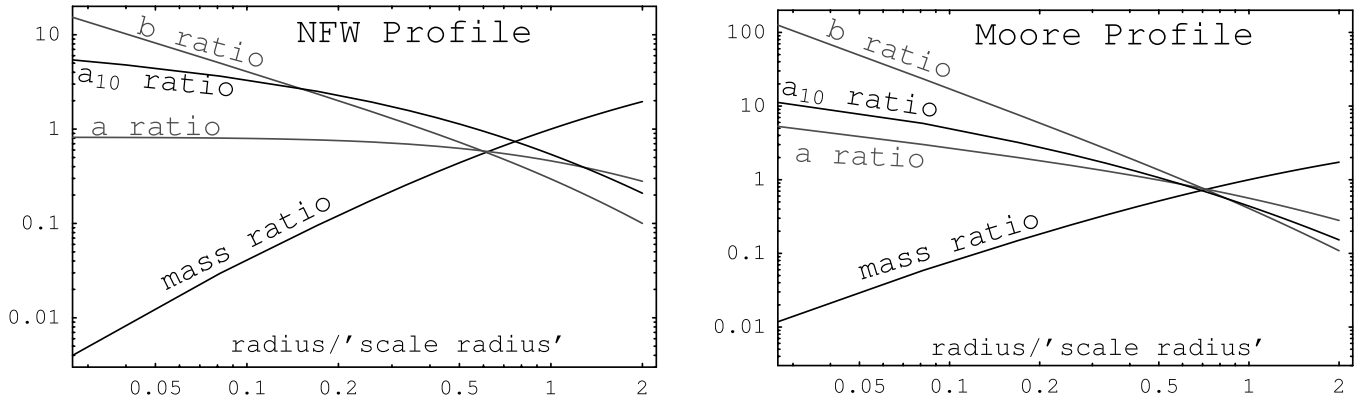

FIG. 3.—A log-log plot of the enclosed mass and lensing coefficients within a dark matter halo having an NFW profile (*left*) or a Moore profile (*right*). The horizontal scale is in units of the scale radius, r_S. The curve marked "mass ratio" is the enclosed mass divided by the scale mass, M_S. The curves marked as "a ratio" are $[M(r)/r^2 - \pi\Sigma]/(M_S/r_S^2)$, the curves marked as "$a_{10}$ ratio" are $\pi\Sigma/(M_S/r_S^2)$, and the curves marked as "b ratio" are $[M(r)/r^3 - \pi\Sigma/r + \pi\Sigma'/4]/(M_S/r_S^3)$. Note the vertical scale change between panels.

finally (3) a model method that takes into account the point-spread function (PSF), the diffusion of charge between camera pixels, the dithering of pointings, and the drizzle of photon counts onto the final pixel grid.

The moment method has the advantage of simplicity, but because the images are necessarily truncated,[9] the accuracy of this method is compromised as a result of edge effects. Pixels not included in the image are usually assumed to have zero counts. Furthermore, this method does not insist that the moments have a radial profile proportional to the derivative of the radial profile of the galaxy, as would necessarily be the case for lensing. The radial-fit method insists that the induced moments arise from the distortion of the radial shape and overcomes edge effects simply by using only nonzero pixels for the fit. When we take into account the PSF and other known processes that distort galaxy images, namely, the charge diffusion and image composition, we refer to the method as the model method. The model method begins with a parameterized radial profile of the source galaxy and proceeds to model the entire image formation process including the PSF, charge diffusion, and image composition. This latter method is limited only by the imperfect knowledge of the features it seeks to include (such as the PSF and charge diffusion), plus, of course, the noise inherent in background galaxy shapes and photon counting noise.

We wish to emphasize that the radial-fit and model methods do not contain an implicit assumption of azimuthal symmetry for the background galaxies. One can imagine applying either of these methods to an unlensed galaxy and finding nonzero map

[9] SExtractor was used to select galaxy images. The sky level is subtracted out. Pixels are retained whose counts after this subtraction are more than either 4 or 6 times the σ of the sky level.

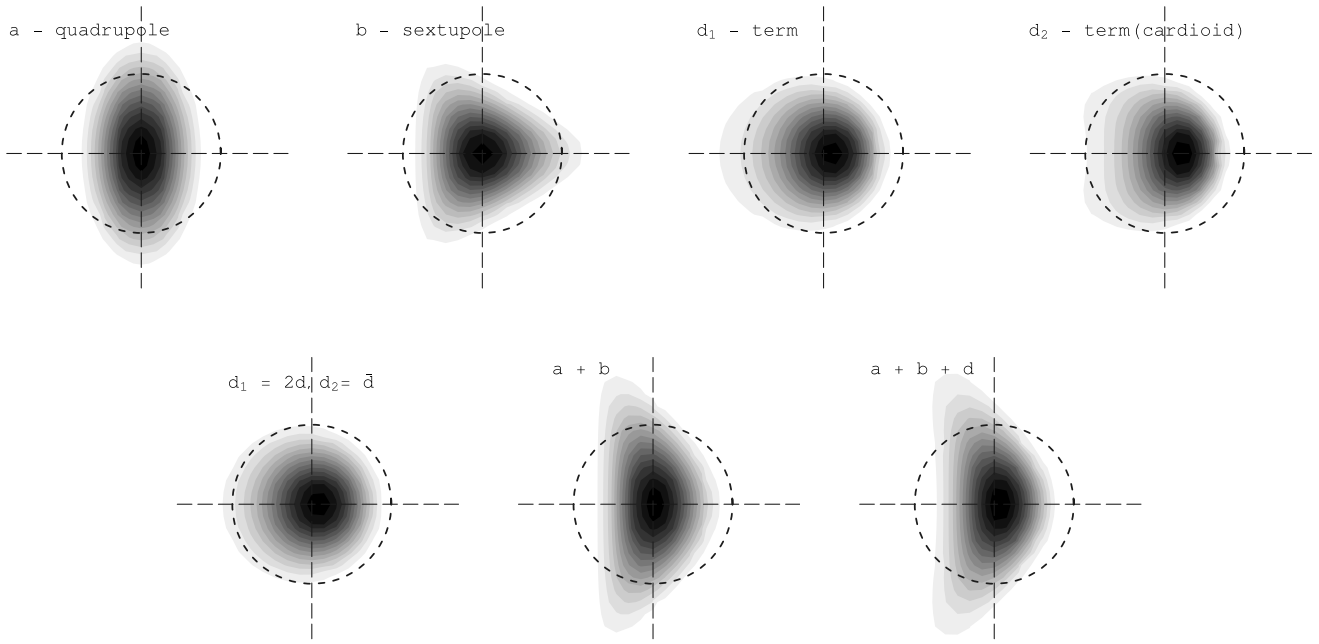

FIG. 4.—Shape deformations coming from different terms of a map. The dashed circles correspond to an original isophote. The top panels demonstrate the deformation due to the presence of single terms: either $a_x = 0.3$, $b_x = -0.06$, $d_{1x} = 0.08$, or $d_{2x} = 0.1$. The bottom panels demonstrate the shape deformation due to combinations of the terms with coefficients (1) ($d_{1x} = 0.03, d_{2x} = 0.015$), (2) ($a_x = 0.3, b_x = -0.045$), and (3) ($a_x = 0.3, b_x = -0.045, d_{1x} = 0.03, d_{2x} = 0.015$). The coefficients of case 2 could be from a point lensing mass. The coefficients of case 3 would come from a distributed lensing mass. [*See the electronic edition of the Journal for a color version of this figure.*]

coefficients a_S and b_S. Then, as shown in § 3.4, if that same galaxy is later lensed, one obtains map coefficients $a \approx a_S + a_L$ and $b \approx b_S + b_L$, where a_L and b_L are the coefficients of the quadrupole and sextupole terms in the lensing map. In general, one would not know whether a and b arose from lensing or from the original shape. However, we are proposing to use the alignment of the quadrupole and sextupole minima to select a subset of background galaxies as having a "lensed" feature. By the study of the clumping of these selected galaxies, one might hope to establish that the sample so selected indeed can be distinguished from randomly selected subsets.

3.1. *Moment Method*

Image moments are defined by the integrals

$$M_{nm} = \int w^n \bar{w}^m i(x,y)\, dx\, dy, \tag{12}$$

where $i(x,y)$ is the light intensity function normalized to a unit integral. According to the notation introduced in § 2, we distinguish the original source galaxy intensity by the subscript S and the intensity as observed at the telescope by the subscript T. Because of the symplectic nature of the lensing map, these intensities are related to one another by $i_S(x_S, y_S)\, dx_S\, dy_S = i_T(x_T, y_T)\, dx_T\, dy_T$. Using this relationship, one can relate the moments of the source to the moments of the observed image through

$$\begin{aligned} M^S_{nm} &= \int w_S^n \bar{w}_S^m i_S(x_S, y_S)\, dx_S\, dy_S \\ &= \int (w_T + \Delta w)^n (\bar{w}_T + \overline{\Delta w})^m i_T(x_T, y_T)\, dx_T\, dy_T, \end{aligned} \tag{13}$$

where $\Delta w = a\bar{w}_T + b\bar{w}_T^2 + 2dw_T\bar{w}_T + \bar{d}w_T^2$. We have set $d = a_{11}/2 = \bar{a}_{20}$, assuming a single lensing plane. See the last paragraphs of § 3.4 below for a discussion of the determination of d-terms.

Inserting this expression for Δw into the expression for M^S_{20}, one can find the following equation for the quadrupole map coefficient:

$$\begin{aligned} M^S_{20} &= \int (w_T + a\bar{w}_T + \ldots)^2 i_T(x_T, y_T)\, dx_T\, dy_T \\ &\approx M^T_{20} + 2aM^T_{11} + a^2 M^T_{02}. \end{aligned} \tag{14}$$

Since the moments on the right-hand side of this equation can be measured from the telescope image (overlooking for the moment the serious problems arising from truncation errors), one obtains a quadratic equation for a depending on the value of M^S_{20}, which, lacking any information of its value, is usually set equal to zero. Since $w\bar{w} = r^2$, it follows that M^T_{11} is the mean square radius of the telescope image. Solving for a,

$$a \approx -\frac{\Delta M_{20}}{2M^T_{11}} \frac{2}{1 + \sqrt{1 + \Delta M_{20}\bar{M}_{20}/M^{T2}_{11}}}, \tag{15}$$

where $\Delta M_{nm} \equiv M^T_{nm} - M^S_{nm}$.

Likewise, an equation for the sextupole moment can be found by inserting the expression for Δw into the expression for M^S_{30}, yielding

$$M^S_{30} \approx M^T_{30} + 3bM^T_{22} + 3aM^T_{21} + \ldots,$$

whence

$$b \approx -\frac{\Delta M_{30}}{3M^T_{22}} - \frac{aM^T_{21}}{M^T_{22}}. \tag{16}$$

To get an expression for the d-term, we insert Δw into an expression for M^S_{21}, resulting in

$$M^S_{21} = M^T_{21} + 2a\bar{M}^T_{21} + \bar{a}M^T_{30} + 5dM^T_{22} + \ldots,$$

yielding

$$d \approx -\left(\Delta M^T_{21} + 2a\bar{M}^T_{21} + \bar{a}M^T_{30}\right)\frac{1}{5M^T_{22}}. \tag{17}$$

If the image were not truncated, it would be possible to extend this method to expressions for the moments in the presence of a PSF. The resulting corrections to the moment equations provide insight into the magnitude of PSF corrections. Intensity functions that have been convolved with the PSF and moments derived from these functions will be designated by a hat. Let p be the point-spread function. Then

$$\begin{aligned} \hat{M}^T_{nm} &= \int w_T^n \bar{w}_T^m \hat{i}_T(x_T, y_T)\, dx_T\, dy_T \\ &= \int\int w_T^n \bar{w}_T^m p(\boldsymbol{r}_T - \boldsymbol{r}'_T) i_T(\boldsymbol{r}'_T)\, dx_T\, dy_T\, dx'_T\, dy'_T \\ &= \int\int \left(\Delta w_T + w'_T\right)^n \left(\Delta\bar{w}_T + \bar{w}'_T\right)^m \\ &\quad \times p(\Delta\boldsymbol{r}_T) i_T(\boldsymbol{r}'_T)\, d\Delta x_T\, d\Delta y_T\, dx'_T\, dy'_T. \end{aligned} \tag{18}$$

Here $\Delta x_T \equiv x_T - x'_T$, etc. When the binomial expressions are expanded, the double integral reduces to the sum of a product of single integrals. One finds, for example,

$$\begin{aligned} \hat{M}^T_{20} &= M^P_{20} + M^T_{20}, \quad \hat{M}^T_{30} = M^T_{30} + M^P_{30}, \\ \hat{M}^T_{21} &= M^T_{21} + M^P_{21}, \quad \hat{M}^T_{11} = M^P_{11} + M^T_{11}, \\ \hat{M}^T_{22} &\approx M^T_{22} + 2M^P_{11}M^T_{11} + M^P_{22}. \end{aligned} \tag{19}$$

In all cases, if the moments of the point-spread function are known, the moments of the original image can be found from the smeared image.

Finally, using the approximations $\hat{a} \equiv -\hat{M}^T_{20}/2\hat{M}^T_{11}$ and $a^P \equiv -M^P_{20}/2M^P_{11}$ and similar approximations for $\hat{b}$ and b^P, and using the relationships of equation (19), one can find an approximation for the map coefficients "before PSF,"[10]

$$a = \frac{1}{\lambda^T_1}\left(\hat{a} - \lambda^P_1 a^P\right), \quad b = \frac{1}{\lambda^T_2}\left(\hat{b} - \lambda^P_2 b^P\right), \tag{20}$$

where

$$\lambda^X_1 \equiv \frac{M^X_{11}}{M^T_{11} + M^P_{11}}, \quad \lambda^X_2 \equiv \frac{M^X_{22}}{M^T_{22} + 2M^T_{11}M^P_{11} + M^P_{22}}.$$

[10] We remind the reader that these are rather poor approximations and often inaccurate for truncated or large galaxy images, and a poor approximation for the PSF because the PSF moments can have rather substantial contributions from large radii.

3.2. *Radial-Fit Method*

We assume a radial profile for the background galaxy of the form[11]

$$F(r_S^2) = (A + Br_S^2 + Cr_S^4)_+ e^{-Dr_S^2}. \quad (21)$$

This will be adequate, since this function must depend only on r_S^2, and we have a parameter (A) for the strength at the center of the galaxy, a parameter (B) that allows for an arbitrary quadratic behavior at the origin, a cutoff parameter (D) that reflects the image size, and a parameter (C) that can modify the behavior as one approaches the cutoff. The plus subscript indicates that if the polynomial has a value less than zero, it is to be set equal to zero. This is necessary to avoid negative intensities, which would be unphysical.[12] Given a centroid, one can numerically determine the radial profile of a galaxy (e.g., by dividing each pixel into many smaller pixels), and this may be compared with the fit results. In cases we have examined, the two curves are indistinguishable.

For convenience, we introduce two additional parameters: each occurrence of r_S^2 is replaced by $(r_S/r_0)^2$, and the polynomial is multiplied by a constant c_0,

$$F(r_S^2) = c_0(A + Bs + Cs^2)_+ e^{-Ds}, \quad (22)$$

where

$$s = \left(\frac{r_S}{r_0}\right)^2.$$

Here r_0 is taken to be near the rms size of the source image. By changing the size of r_0, one can change the size of the image without affecting its shape. The factor c_0 is introduced so that the shape parameters, which are now dimensionless, have values $A \approx 1$, and B and C can be compared to unity.

The effect of lensing is contained in the parameters of the map of equation (5). One replaces each occurrence of r_S^2 by the expression $w_S\bar{w}_S$.

The parameters of the radial profile and the map are determined by minimizing the L2 norm,

$$||i_F - i_T||_\omega^2 = \int (i_F - i_T)^2 \omega \, dx_T \, dy_T, \quad (23)$$

where

$$i_F = F(r_S^2)\left|\frac{\partial w_S}{\partial w_T}\right|.$$

In i_F, $r_S^2 = w_S\bar{w}_S$ is understood to be a function of x_T and y_T through w_T and $\bar{w}_T$. The term with vertical bars is the Jacobian of the transformation between S and T variables (the same as in eq. [4]). To avoid a strong coupling between the shape variables and the map variable a, the Jacobian is divided by the quantity $1 - |a|^2$, essentially incorporating this factor in the scaling variable c_0. A weight function ω can be introduced if desired. However, because this technique ignores truncated pixels rather than taking them to be zero, edge effects are inherently smaller as compared to the moment method. At each calculation of i_F, the Jacobian is monitored to see that it does not change sign between that point and the origin along a radial line.

With parameters a, b, and d included in the map, together with the centroid position, w_0, and the shape parameters A, B, C, and D, there are 12 variables to determine. The fit is done in several steps using a multidimensional Newton's method. At each step any subset of the 12 variables is allowed to vary. The curvature matrix for these parameters is computed, then diagonalized, and eigenvectors with very small eigenvalues are not allowed to contribute to the function change at that step. The convergence to a minimum is controlled by a parameter step size.

The map parameters are not strictly orthogonal, but because of their distinct angular behavior, they appear to be stable and well determined. See § 6.5 for a rigorous discussion of the accuracy of this parametric fit using Fisher matrices.

3.3. *Model Method*

The model method begins by constructing an i_F as in § 3.2 (here on 0.″02 pixels) and convolving it with a subsampled PSF (also on 0.″02 pixels), as provided by the Tiny Tim[13] program. This convolved image is dropped (25 times) onto a 5×5 dithered original pixel grid (0.″1 pixels). A diffusion kernel,

$$K = \begin{bmatrix} 0.025 & 0.05 & 0.025 \\ 0.05 & 0.70 & 0.05 \\ 0.025 & 0.05 & 0.025 \end{bmatrix}, \quad (24)$$

is applied to each resulting image. The footprint of each original pixel is shrunk to half its size in each dimension and then "drizzled" to the final Hubble Deep Field grid (0.″04 pixels) according to the intersection of the diminished original pixel area with the pixels in the final grid. We do not attempt to reproduce the actual offsets of the dithers of the original camera. The actual process has nine dithers, whose offsets vary across the field. We are content to capture the main features of the dither, diffusion, and drizzle process. Ultimately, one would prefer to avoid the drizzle operation and fit the original dithered images directly. The model method is well suited for that.

An additional complication with the model method comes from the Jacobian condition given the fact that a and b for the fit to the source are typically larger by a factor of about 2 as compared to the radial-fit method. In the case in which we are fitting only the a and b map parameters, the Jacobian is given by $1 - |a + 2b\bar{w}_T|^2$, which as for the radial-fit method is divided by $1 - |a|^2$. For fixed radius r the condition on positivity for all angles θ becomes $|a| + 2|b|r \leq 1$. We have introduced an additional cut, of the form $|a| + 2|b|r_{\max} \leq 1$, for which it was necessary to remove only three additional images.

3.4. *Map Form and Interpretation*

In both the radial-fit and model methods one fits the radial shape parameters and the parameters of the lensing distortion map, in the form

$$w_S = w_T + a\bar{w}_T + b\bar{w}_T^2 + d_1 w_T \bar{w}_T + d_2 w_T^2 + \ldots. \quad (25)$$

In this section we discuss the implication of the choice of unity for the coefficient of w_T and what information is actually contained in the remaining coefficients, given that the background galaxy shape can affect the outcome. The results of this section are important in constructing simulations.

[11] Kuijken (1999) introduced the radial-fit method, taking a sum of Gaussians as the *Ansatz* for the radial profile.

[12] The fit method we use requires an analytic expression for the derivative of the fit function. Fortunately, $(Q_+)' = [Q\Theta(Q)]' = Q'\Theta(Q)$, since the value of the polynomial, Q, is zero where the step function $\Theta(Q)$ has a nonzero derivative.

[13] See http://www.stsci.edu/software/tinytim.

To begin the discussion, let us assume that the background galaxy is azimuthally symmetric and that we have a lensing map of the form $w_S = \lambda w_T + a_L \bar{w}_T$, with $\lambda = |\lambda| e^{i\phi_\lambda}$. This map can be written as the composition of two maps, in the form

$$w_S = \lambda w_{S'}, \quad w_{S'} = w_T + \frac{a_L}{\lambda} \bar{w}_T, \tag{26}$$

since plugging the second map into the first map will reproduce the initial lensing map. However, the first map is a simple scale change plus a (invisible) rotation of the initial azimuthally symmetric initial shape, taking r_S into $|\lambda| r_{S'}$ and θ_S into $\theta_S + \phi_\lambda$. The scale change would also not be detectable, and hence this map would be completely invisible to us. The second map is of the form proposed, and we see that on comparing with equation (25), the parameter identified as a is actually a_L/λ. This is sometimes referred to as "reduced shear" and provides the interpretation for the a-parameter of the map.

Now let us assume that the initial galaxy was not round, but that we somehow had access to it. We can find all the information we need for this galaxy by assuming that there is an azimuthally symmetric "root" galaxy that has been mapped into this shape observed. In other words, we assume a map of the form $w_R = w_S + a_S \bar{w}_S$ and determine a_S by using the radial-fit or model method applied to the background (source) galaxy. In this way we characterize the background galaxy by the parameter of concern to us.

We then factor the lensing map as above, concatenate the scaling map with the source map (plug one into the other), and then take out the scaling as we did before. In this way the scaling is moved to the front, and the linear source map remains unchanged. Again, the scaling, acting on the round root galaxy, is invisible. The remaining maps can be concatenated to give

$$w_R = (1 + a_S \bar{a}'_L) w_T + (a_S + \bar{a}'_L) \bar{w}_T, \tag{27}$$

where we have defined $a'_L \equiv a_L/\lambda$. We see that another scaling has appeared, which is now factored out to obtain

$$w'_R = w_T + (1 + a_S \bar{a}'_L)^{-1} (a_S + \bar{a}'_L) \bar{w}_T. \tag{28}$$

We can read off the desired expression for a: the result is a factor near unity times $a_S + \lambda^{-1} a_L$. Even for relatively strong lensing with $|a_L| = 0.4$ and $|a_S| = 0.4$, the factor remains within 16% of unity.

When the sextupole-order terms are included, all goes through in an identical fashion, except for the fact that when the scaling gets moved through the source map, the second-order coefficients of the source map get multiplied by λ. With all factors included, the results are

$$\begin{aligned}
a &= \left(1 + a_S \bar{a}'_L\right)^{-1} \left(a'_L + a_S\right), \\
b &= \left(1 + a_S \bar{a}'_L\right)^{-1} \left(b'_L + b'_S + a'_L d'_{1S} + a_S d'_{2L} + a'^2_L d'_{2S}\right), \\
d_1 &= \left(1 + a_S \bar{a}'_L\right)^{-1} \left[d'_{1L} + d'_{1S}\left(1 + \left|a'_L\right|^2\right) + 2\bar{a}'_L b'_S + 2a'_L d'_{2S}\right], \\
d_2 &= \left(1 + a_S \bar{a}'_L\right)^{-1} \left(d'_{2L} + d'_{2S} + a_S \bar{b}'_L + \bar{a}'^2_L b'_S + \bar{a}'_L d'_{1S}\right).
\end{aligned} \tag{29}$$

As above, a'_L, b'_L, d'_{1L}, and d'_{2L} are the original lensing map coefficients divided by λ. The quantities b'_S, d'_{1S}, and d'_{2S} are the original source map coefficients multiplied by λ. To first order, we find that $a \approx a_L + a_S$ and $b \approx b_L + b_S$. Since $|\lambda|$ is almost surely smaller than unity,[14] its impact is to enhance all the lensing coefficients and diminish the second-order source coefficients.

Estimates for the size of the background coefficients will come out of our analysis of the entire background galaxy field. To have a meaningful signal for sextupole lensing, large enough to align the minima of the background moments, the lensing coefficients must have magnitudes as large as the background coefficients of the lensed galaxy.

Since the radial shape involves only $r_S^2 = w_S \bar{w}_S$, one finds that it depends only on

$$\begin{aligned}
r_S^2 = &\left(1 + |a|^2\right) r^2 + 2\mathrm{Re}\left(a\bar{w}^2\right) + 2\mathrm{Re}\left[(b + \bar{a}d_2)\bar{w}^3\right] \\
&+ 2\mathrm{Re}\left[\left(d_1 + \bar{d}_2 + a\bar{d}_1 + \bar{a}b\right) w\bar{w}^2\right] + \ldots .
\end{aligned} \tag{30}$$

Here the $\bar{w}^2$ term has a distinctive $e^{-i2\theta}$ behavior, the $\bar{w}^3$ term has a distinctive $e^{-i3\theta}$, and the $w\bar{w}^2$ term has a distinctive $e^{-i\theta}$ behavior, implying that a, b, and $(d_1 + \bar{d}_2 + a\bar{d}_1)$ are well determined. We are assuming that $|ad_2| \ll |b|$, which is valid in preliminary studies assuming that d_1 and d_2 are related by the lensing condition $d_1 = 2\bar{d}_2$. The d_1 and d_2 dependence occurs in a different linear combination as linear coefficients of $re^{-i\theta}$ in the Jacobian, creating a linear tilt that acts somewhat like a dipole kick. In this way, the apparent degeneracy between d_1 and d_2 is removed for significant strengths.

4. GALAXY PROPERTIES

The software SExtractor (Bertin & Arnouts 1996) was used to select galaxies from the Hubble Deep Field–North and to specify which pixels to include in the image. Galaxies were selected that appeared for both a 4 $\sigma_{\rm sky}$ and a 6 $\sigma_{\rm sky}$ threshold option (4 or 6 times the σ of the sky noise) with the convolution option taken to be the identity. Only galaxies that had been assigned a z-value with $z > 0.8$ were kept as background galaxies.[15] There were 569 galaxies so identified in the north field.

Galaxy images were transferred to the *Mathematica* programming environment for inspection, where galaxies with more than one maximum were removed. Of the 569 identified galaxies with $z > 0.8$, 427 survived this single-maximum cut. The total (recorded) photon count[16] and peak height of the surviving galaxies are shown in Figure 5, and the total area and rms radius are shown in Figure 6.

5. QUADRUPOLE COEFFICIENT MEASUREMENTS

5.1. *Quadrupole Coefficients from Moment and Radial-Fit Methods*

In Figure 7 (*left*) we compare the distributions of the magnitudes of the quadrupole coefficients using the moment method and the radial-fit method. The ranges of magnitudes are surprisingly similar. This can only occur if the fit to the radial profile results in an M_{20}^T moment that is significantly smaller than the integrated moment, because if M_{20}^T were arising dominantly from the distortion of an originally radial galaxy profile, one could derive a simple analytic expression for the magnitude of this

[14] Since $\lambda = 1 + a_{10}$ and a_{10} is negative, $|\lambda| < 1$ until $|a_{10}| > 2$. For this to be true, the centroid trajectory must be within the Einstein radius at a point where the local mass density is twice the average density within the Einstein radius.

[15] We used z-catalogs from http://www.ess.sunysb.edu/astro/hdf.html.

[16] The counts are actually "recorded" photons.

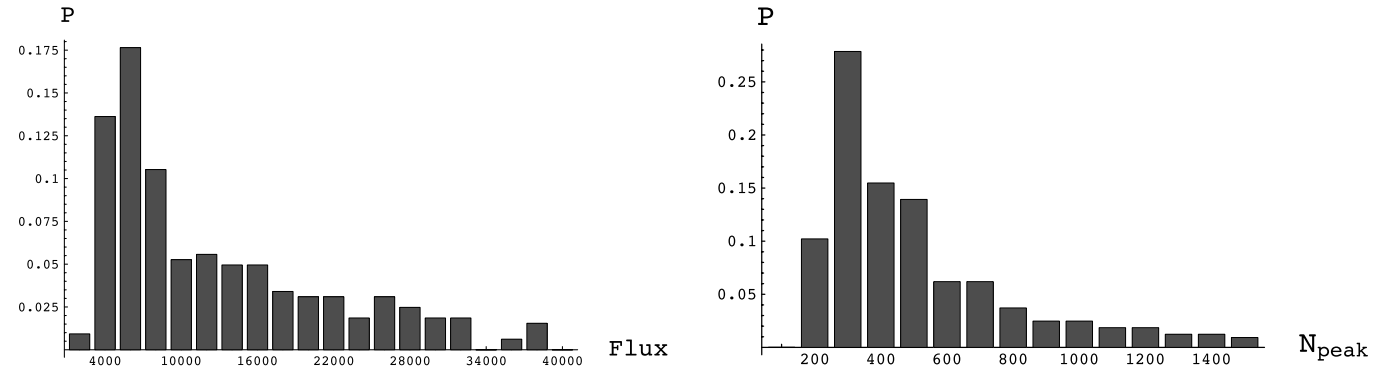

FIG. 5.—*Left:* Distribution of total photon counts for all galaxies in the HDF-N with $z \geq 0.8$, identified by SExtractor with intensity exceeding 6 $\sigma_{\rm sky}$, and having a single major maximum. *Right:* Photon count of the peak pixel for the same galaxies. [*See the electronic edition of the Journal for a color version of this figure.*]

moment, even when truncated. To see this, consider the following expression for one component of M_{20}^T:

$$\begin{aligned}
\mathrm{Re}\left(M_{20}^T\right) &= \int r^2 \cos 2\theta i_S\left(r_S^2\right)\left|\frac{\partial w_S}{\partial w_T}\right| dA \\
&\approx \int r^2 \cos 2\theta \\
&\quad \times \left[i_S\left(r^2\right) + 2r^2\left(a_x \cos 2\theta + a_y \sin 2\theta\right)\frac{di_S}{dr^2} + \ldots\right] r\, dr\, d\theta \\
&\approx 2\pi a_x \int r^4 \frac{di_S}{dr^2}\, dr^2 \\
&\approx -2a_x \int r^2\left[i_S\left(r^2\right) - i_S\left(r_B^2\right)\right] dA = -2a_x \underline{M}_{11}^T. \qquad (31)
\end{aligned}$$

In the first line here we have set $x^2 - y^2 = r^2 \cos 2\theta$. In the second and third lines we have expanded the function $i_S(r_S^2)$ about $r^2 \equiv r_T^2$, assuming that a_x and a_y are small. We also set $dA = r\, dr\, d\theta$. In the fourth line we integrate over θ. Only the integral over $\cos^2 2\theta$ survives. Next we integrate by parts with respect to the variable r^2. The boundary term at the origin vanishes by virtue of the r^4. The boundary term at the outer boundary, which for the purposes of this estimate is assumed to be a disk of radius $r = r_B$, is $r_B^4 i_S(r_B^2)$, which we have chosen to write as $2i_S(r_B^2)\int r^2\, dr^2$.

The resulting final integral is over the footprint of the disk, but we interpret this generally as the footprint of the truncated image. The underline in $\underline{M}_{11}^T$ indicates that the integrand is to be defined as the photon count in excess of the truncation floor. We call this an "above-floor" moment. The equation can now be solved for a_x with a result that is satisfyingly simple and directly comparable with the result found using the moment method, as in equation (14): the denominator M_{11}^T is simply replaced by $\underline{M}_{11}^T$. Similar results can be found for the other moments, which we summarize here for future reference:

$$a \approx -\frac{M_{20}^T}{2\underline{M}_{11}^T}, \quad b \approx -\frac{M_{30}^T}{3\underline{M}_{22}^T}, \quad d \approx -\frac{M_{21}^T}{9\underline{M}_{22}^T - 4M_{22}^T}. \qquad (32)$$

The irregularity in the expression for d arises from the linear dependence on d in the Jacobian.

Since the above-floor denominators could be significantly smaller than the expressions used in the straight moment method, these estimates for map coefficients could be significantly larger. However, based on our results using the radial-fit method, which does indeed insist on such a relationship, one can only draw the conclusion that an equally large part of the moment M_{20}^T is not coming from the distortion of the radial profile and that these effects pretty much cancel one another. This is an interesting result and indicates that the radial-fit method is indeed an important tool in making such a distinction. We would assert that a substantial amount of noise is projected out with the radial method. This could be important for high-resolution weak-lensing surveys such as the *Supernova/Acceleration Probe* (*SNAP*).

The orientation of moments is more important to us than their magnitude, because we are using the orientation to distinguish curved from aligned galaxies. Figure 7 (*right*) compares the map coefficient orientation of the radial-fit method with the moment

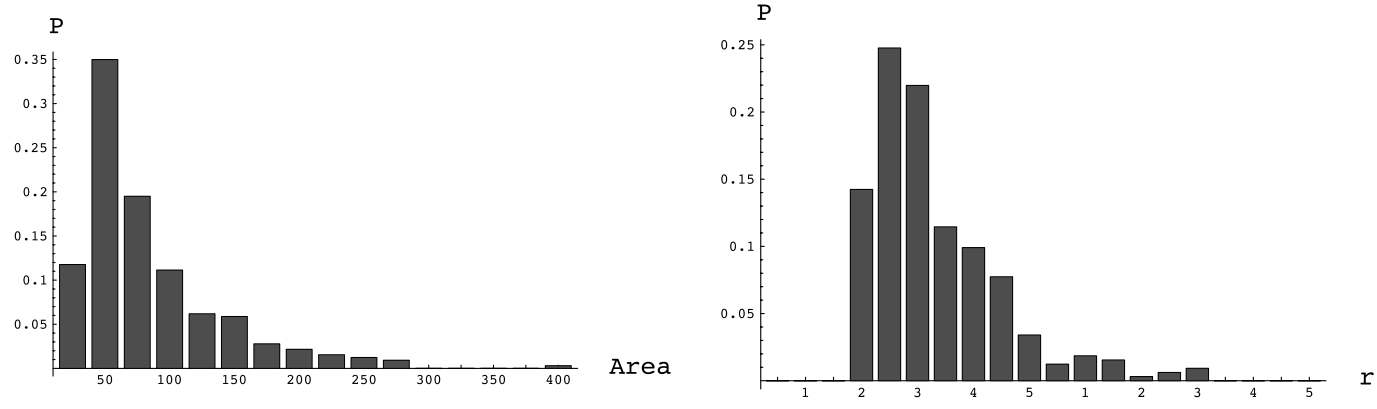

FIG. 6.—Distribution of galaxy areas (*left*) and distribution of galaxy rms radii (*right*) for the galaxy set described in Fig. 5 above. Units for both plots are pixels. [*See the electronic edition of the Journal for a color version of this figure.*]

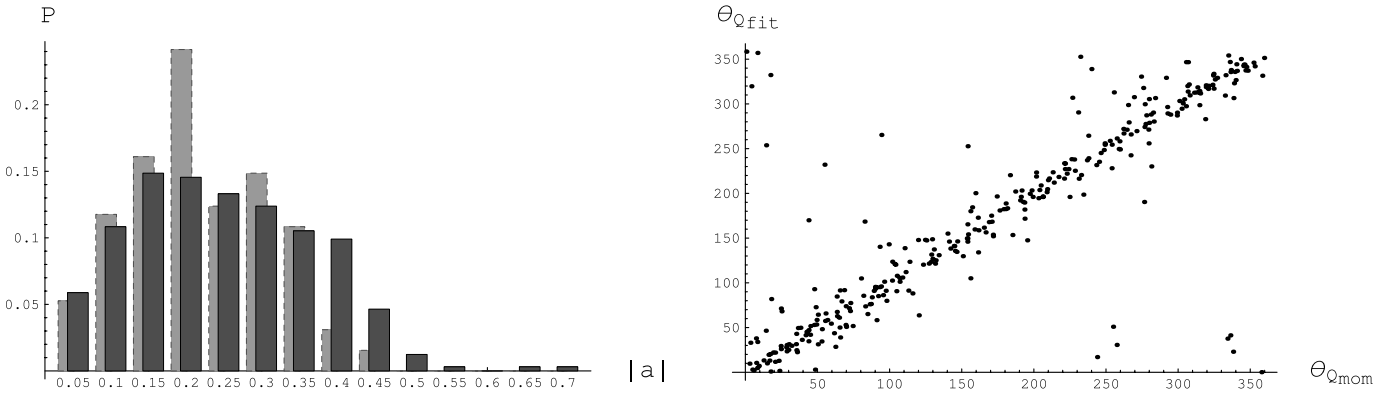

FIG. 7.—Distribution of the quadrupole map coefficient for all galaxies in the set described in Fig. 5, for both the moment method (*background*) and the radial-fit method (*foreground*; *left*), and comparison of the angular orientation of the quadrupole map coefficient for the moment method and the radial-fit method (*right*). [*See the electronic edition of the Journal for a color version of this figure*.]

method. We would like to establish the orientation of the resulting elliptical shape within 10°.[17] Since the quadrupole map coefficient advances by 2ϕ as the ellipse rotates by ϕ, the relevant limit for the determination of ϕ is 20°. One can see in Figure 7 that although there is considerable agreement between the angle differences between these two methods, the quadrupole map coefficient differences are often larger than 20°.

5.2. *Analytical Quadrupole Noise Estimates*

The first formula of equation (32) can be used to derive a Poisson noise estimate for the quadrupole coefficient, $a_{\rm fit}$, derived from the fit method. An estimate for the contribution of Poisson noise to M_{20} is required. For each component, this can be obtained from the integral

$$\begin{aligned}\mathrm{Re}\left(M_{20}^T\right) &= \frac{\int r^2 \cos 2\theta\zeta\sqrt{n(r,\theta)+\sigma_{\rm sky}^2}\,dA}{\int n(r,\theta)\,dA}\\ &\approx \frac{1}{N}\sqrt{\int r^4\cos^2 2\theta\left[n(r,\theta)+\sigma_{\rm sky}^2\right]\,dA}\\ &= \sqrt{\frac{M_{22}^T}{2N}+\frac{N_{\rm sky}\mathcal{R}^4}{2N^2}},\end{aligned} \tag{33}$$

where ζ is a stochastic variable, $n(r,\theta)$ is the number of counts for each pixel, N is the total number of counts for the image, $\sigma_{\rm sky}^2$ is the variance of the sky noise, $N_{\rm sky}=\sigma_{\rm sky}^2 A$, and $\mathcal{R}^4 = \int r^4\,dA/A$. Here $[n(r,\theta)+\sigma_{\rm sky}^2]^{1/2}$ appears as an estimate for the counting noise in the pixel at (r,θ). In the second line the weak θ behavior of $n(r,\theta)$ is ignored. Similar formulae hold for the other map coefficients. We summarize the results as

$$\begin{aligned}|a_{xN}| &\approx \sqrt{\frac{M_{22}^T}{2N}+\frac{N_{\rm sky}\mathcal{R}^4}{2N^2}}\,\frac{1}{2\underline{M}_{11}^T},\\ |b_{xN}| &\approx \sqrt{\frac{M_{33}^T}{2N}+\frac{N_{\rm sky}\mathcal{R}^6}{2N^2}}\,\frac{1}{3\underline{M}_{22}^T}.\end{aligned} \tag{34}$$

The subscript x indicates that this is an estimate for one component, which could be in any direction, of course. It is a minimum estimate, in the sense that only the Poisson counting noise is being included. For example, contributions to the noise from edge effects are not included.

The actual $|a|$ should be large enough so that if the perpendicular component to a were changed by an amount $|a_{xN}|$, the angle would change by less than the required resolution on angles. The magnitude of the relative orientation of the quadrupole and sextupole shapes (δ in Fig. 1) runs from 0° to 30°. Since we choose to designate curved galaxies as those for which $|\delta|<10^\circ$, aligned galaxies as those for which $|\delta|>20^\circ$, and midrange galaxies as the remaining ones, and considering positive as well as negative signs for δ, the regions describing curved and aligned galaxies are actually 20° wide. Hence, we may take 10° ($=0.17$ rad) as an estimate for the required resolution on δ. Since δ is the difference between the orientation of the quadrupole and sextupole shapes, the resolution on δ could be achieved by requiring the sum of the resolution squared of each shape individually to be less than $(0.17)^2$. As the shapes rotate by ϕ, the quadrupole map coefficient angle changes by 2ϕ, and the sextupole map coefficient angle changes by 3ϕ. Thus, this resolution condition on $a_{\rm fit}$ and $b_{\rm fit}$ could be written

$$\left(\frac{1}{2}\tan^{-1}\left|\frac{a_{xN}}{a_{\rm fit}}\right|\right)^2+\left(\frac{1}{3}\tan^{-1}\left|\frac{b_{xN}}{b_{\rm fit}}\right|\right)^2<(0.17)^2. \tag{35}$$

We could choose to satisfy this condition by requiring that the quadrupole contribution be less than $6\overset{\circ}{.}3$ and the sextupole

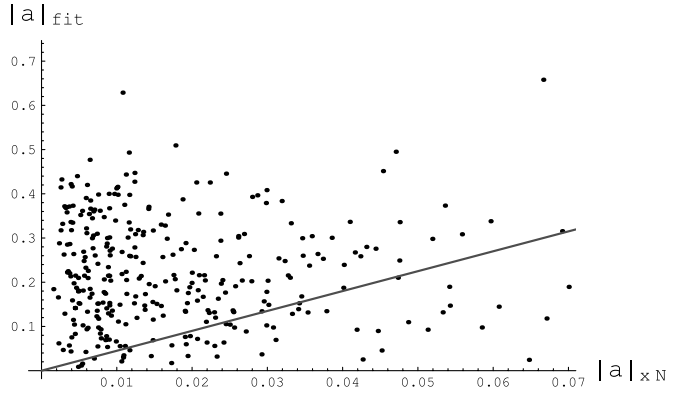

FIG. 8.—Plot of the quadrupole Poisson noise estimate (*horizontal axis*) vs. the magnitude of the quadrupole coefficient. The galaxies falling below the straight line with slope 4.5 will be cut as having signal-to-noise ratios too small. [*See the electronic edition of the Journal for a color version of this figure*.]

[17] Based on Poisson noise estimates, we have divided up the 30° range of the smallest angle between a quadrupole minimum and a sextupole minimum into three equal increments of 10° and referred to them as curved, midrange, and aligned galaxies.

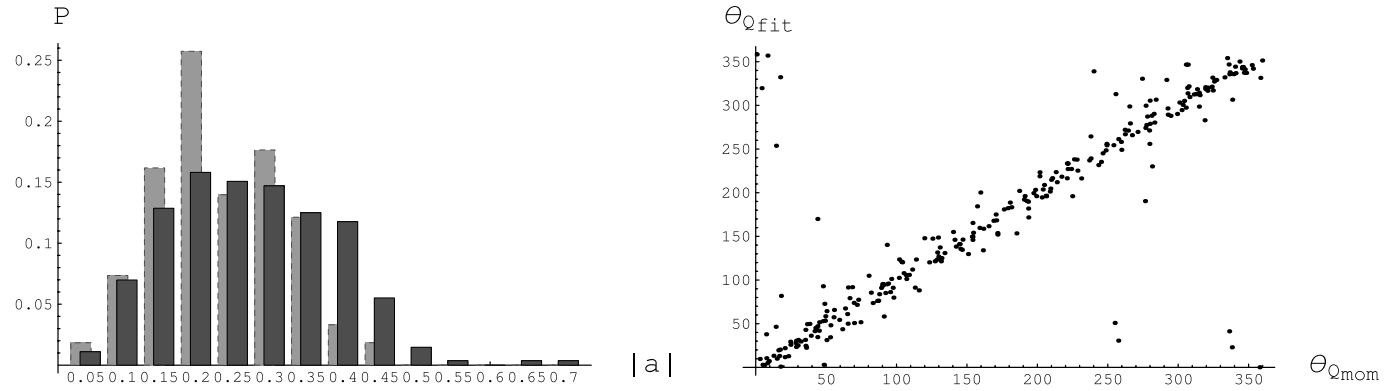

FIG. 9.—Comparison, after signal-to-noise cut, of the magnitude of the quadrupole map coefficient for both the moment method (*background*) and the radial-fit method (*foreground*; *left*) and of the angular orientation of the quadrupole map coefficient for the moment and the radial-fit methods (*right*). Compare with Fig. 7. [*See the electronic edition of the Journal for a color version of this figure.*]

contribution be less than 7°.8. The quadrupole cut would then be equivalent to requiring that $|a| > 4.5|a_{xN}|$, and the sextupole cut would be equivalent to $|b| > 2.3|b_{xN}|$. The results of the quadrupole cut are shown in Figure 8, where the vertical axis is the quadrupole strength and the horizontal axis is the estimated Poisson noise from the leading term in equation (34) for that galaxy. The straight line is the cut condition, and galaxies below this line would be rejected as having a signal-to-noise ratio that is too small.

In Figure 9 we show the comparison between the moment and radial-fit methods after this signal-to-noise cut for magnitude distributions and angle distributions. The orientations using the two methods are now in better agreement.

5.3. *Quadrupole Coefficients from the Model Method*

In Figure 10 (*left*) we show the magnitude of the quadrupole coefficient using the model method. Of the 427 selected galaxies having one apparent maximum, 47 resulted in an L2 norm squared ($\|i_F - i_T\|^2$) greater than 0.05. These galaxies were cut from the sample, for the reason that their shape does not conform sufficiently well to the model we are using to estimate map-coefficient strengths.

The magnitudes of the quadrupole coefficients are almost a factor of 2 larger using the model method than the radial-fit method. This occurs even when $a_{\rm PSF} = 0$, because there is still a dilution of the a parameter. When the rms size of the source galaxies is about equal to the rms size of the PSF, this dilution is about a factor of 2. See equations (19) and (20) in § 3.1.

The rms size of the galaxy image after including the PSF is about 2.7 HDF pixels (see Fig. 6). The half-width at half-maximum of the PSF is about 2.0 HDF pixels, but the rms is larger than that, because the radial profile of the PSF flattens out. In fact, the rms of the PSF is poorly defined, depending on exactly how one cuts off the footprint. For small cutoffs one can easily reach an rms of 2.5 pixels. That implies the average galaxy image before including the PSF is also about 2.5 pixels, and the factor $1/\lambda_T \approx 2$ in equation (20).

Figure 10 (*right*) compares the orientations of the quadrupole map coefficient of the radial-fit method with the model method. The differences are now much smaller. The diffusion, being symmetric, will not change the orientation, but the PSF of the *Hubble Space Telescope* (*HST*) is known to have a substantial quadrupolar component that varies dramatically across the field, making it difficult to do weak lensing with the *HST*.

An example of a 5 times subsampled PSF, as obtained from Tiny Tim, is shown in Figure 11 (*left*). We have specified the F606 filter at the location of each of the 427 galaxies in our sample. There is typically a diffraction ring at a radius of 2 HDF pixels, which contains about 30% of the counts. The radius of the central peak is too small to give significant moments, so the moments of concern arise from the ring.

Figure 11 (*right*) shows this PSF after it has been dithered, diffused, and dropped onto the final *HST* 0.″04 grid. We have taken these PSFs, which have been dithered, diffused, and drizzled, and fit them using the radial-fit method. Figure 12 shows the resulting distribution of the magnitude of the quadrupole

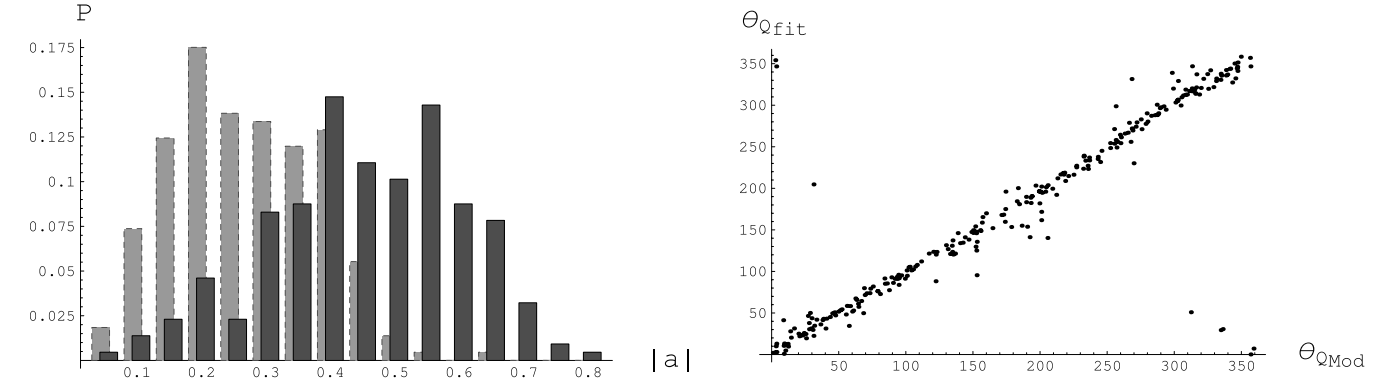

FIG. 10.—Distribution of the magnitude of the quadrupole map coefficients using the model method (*foreground*) compared with the radial-fit method (*background*; *left*) and of the angular orientation of the quadrupole map coefficient for the model and the radial-fit methods (*right*). [*See the electronic edition of the Journal for a color version of this figure.*]

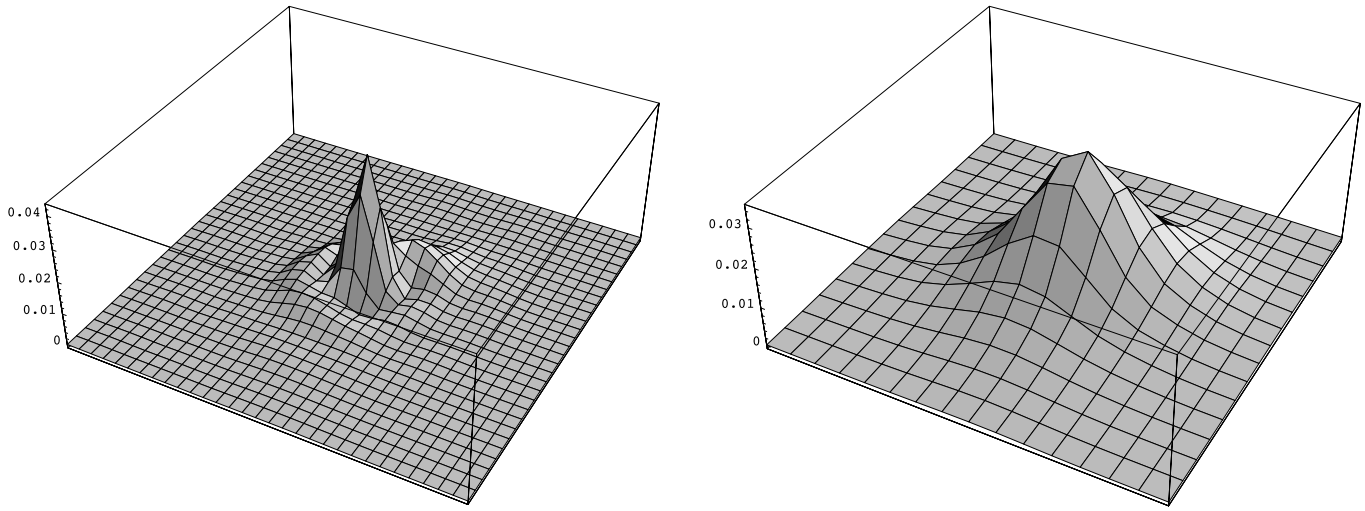

FIG. 11.—*Left:* Picture of a *HST* WFPC2 (Wide Field Planetary Camera 2) PSF as produced by the Tiny Tim program. The pixel size is 5 times smaller than the *HST* camera pixels, in other words, 2 times smaller than the drizzled HDF pixels. *Right:* Same PSF diffused and drizzled. [*See the electronic edition of the Journal for a color version of this figure.*]

coefficients (*right*), as well as their spatial distribution and orientation (*left*).

6. SEXTUPOLE COEFFICIENT MEASUREMENT

6.1. *Sextupole Coefficients from Moment and Radial-Fit Methods*

We now follow the sequence of § 5 for the sextupole coefficient measurements. Figure 13 (*left*) compares the sextupole coefficient magnitudes for the moment method and the radial-fit method. Again, the radial-fit method would have been larger if the entire M_{30}^T arose from a distortion of the radial profile, since the M_{22}^T will typically be much larger than $\underline{M}_{22}^T$. As before, we conclude that the radial-fit method is projecting out a substantial portion of the background-galaxy sextupole moment noise. Figure 13 (*right*) shows a comparison of the sextupole angle measurement for the moment and the radial-fit method. Since for this moment a rotation of the image by ϕ results in a change of the coefficient angle by 3ϕ, an angular difference in the coefficient of 30° is a measure of significance.

6.2. *Sextupole Noise Estimates*

Following the discussion of § 5.2, we require the sextupole angle to change by less than $3 \times 7.^\circ8 = 23.^\circ4$ when the Poisson noise estimate is added perpendicular to the vector representing the sextupole signal. This implies that $|b| > 2.3|b_{xN}|$. In Figure 14 we plot the sextupole strength on the vertical axis versus the sextupole Poisson noise estimate on the horizontal axis. The straight line has a slope of 2.3, showing the cut criteria for sufficient sextupole signal-to-noise ratios. In Figure 15 we show the distribution comparison between the moment and fit methods after this signal-to-noise cut and the angle comparison after

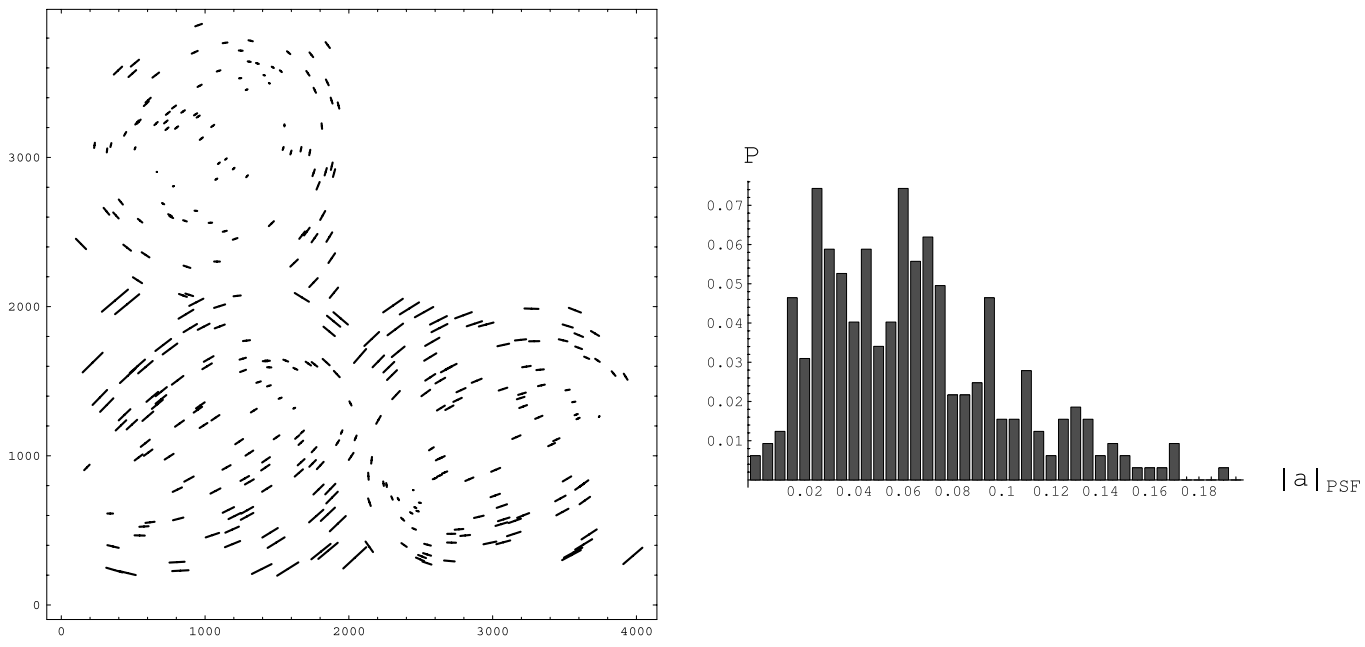

FIG. 12.—Spatial ellipticity distribution (*left*) and the distribution (*right*) of the magnitude of the quadrupole coefficient for the 5 times subsampled and drizzled Tiny Tim PSFs for the WFPC2 on the *HST*. [*See the electronic edition of the Journal for a color version of this figure.*]

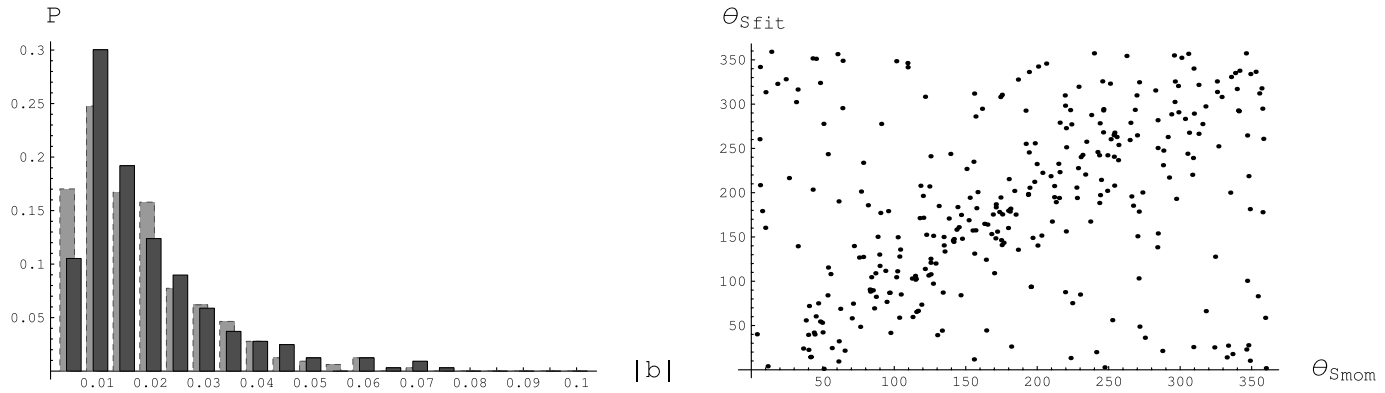

FIG. 13.—*Left:* Distribution of the magnitude of the sextupole map coefficient, for the radial-fit method (*foreground*) and the moment method (*background*). Units are (HDF pixel)$^{-1}$. Multiply by 25 to get units arcsec^{-1}. *Right:* Comparison of the orientation of the sextupole map coefficients for the radial-fit method (*vertical axis*) and the moment method (*horizontal axis*). [*See the electronic edition of the Journal for a color version of this figure.*]

this cut. Clearly, scatter is reduced as compared to Figure 13, indicating that much of the scatter in the angular measurement could be attributed to noise.

Finally, Figure 16 addresses the combination of resolutions that can be expected for a and b, showing the condition formulated above in equation (35). It is this cut that we impose when we consider the relative orientation of the quadrupole and sextupole map coefficients. There are 217 galaxies that survive this cut.

The following list summarizes the results on the several galaxy cuts. For the sequence 1–5, each cut is for the combination of the previous conditions. The cuts give

(1) 569 in the z-catalog with $z > 0.8$ and found by SExtractor for thresholds 4 $\sigma_{\rm sky}$ and 6 $\sigma_{\rm sky}$,
(2) 427 having only one prominent maximum,
(3) 370 larger than 5 pixels in both x and y,
(4) 323 with the radial fit having its L2 squared norm less than 0.05,
(5*a*) 276 with quadrupole signal-to-noise ratios greater than 4.5,
(5*b*) 216 with sextupole signal-to-noise ratios greater than 2.3, and
(5*c*) 217 satisfying the joint-variable signal-to-noise cut condition of equation (35).

Only a very few galaxies had $|a| + 2|b|r_{\rm max} > 1$, so this cut was not enforced. Further signal-to-noise cuts, arising for the d terms, must be combined with the above cuts to establish their orientation with respect to the imputed direction to the scattering center. Since these cause the surviving statistical sample to become uncomfortably small, we postpone a discussion of the relevance of the d terms, if any, to a subsequent paper with larger statistical samples.

6.3. *Sextupole Coefficients from Model Method*

The distribution of the sextupole coefficient magnitudes for the model method is shown in Figure 17 (*left*), and the comparison of the orientation of the sextupole coefficient for the model and radial-fit methods is shown in Figure 17 (*right*). The relevant difference in sextupole angle, as noted above, is 30°. Many galaxies have changed by that amount, indicating the importance of the PSF correction.

Figure 18 (*left*) shows the distribution of sextupole coefficients that were found by computing moments of the PSF after it had been dithered, diffused, and drizzled. The right panel shows the orientation of the sextupole moment, with the lines of each symbol pointing toward the three sextupole shape maxima. Remarkably, the sextupole moment orientation is uniform across each chip. This may be helpful in following time variation of the sextupole coefficient, if any is present.

6.4. *Relative Orientation of the Quadrupole and Sextupole Map Coefficients*

The orientation of the sextupole map coefficient with respect to the quadrupole coefficient is of primary interest to us. A plot of the magnitude of the smallest angle between sextupole and quadrupole minima, using the model method, is shown in Figure 19 for the galaxies surviving both the L2 norm < 0.05 cut and the signal-to-noise cut of equation (35). This angle magnitude, which we refer to as δ, runs from 0° to 30°. For $\delta = 30°$ the shapes will have aligned maxima, and we refer to such galaxies as "aligned." They are pear-shaped galaxies, as compared to the curved galaxies, which resemble bananas. See Figure 1.

Figure 20 compares δ found with the radial-fit and model methods. About one-third of all galaxies show a change in δ of greater than 10°. This is a concern, because it means that the point-spread function does indeed play an important role in distinguishing curved from noncurved galaxies. This would not be as great a concern if the PSF were well known, but unfortunately the PSF is known to vary with time. We return to a discussion of the role of the PSF in § 8.2.

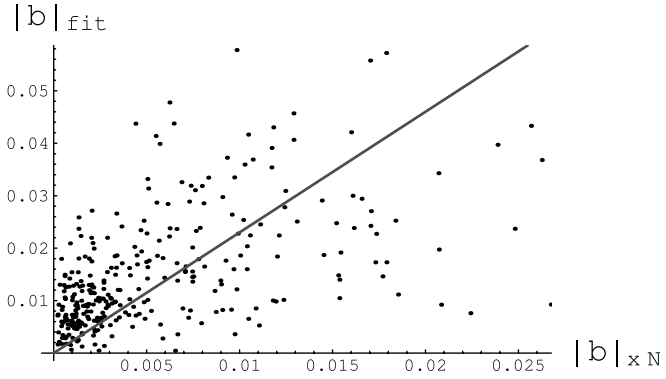

FIG. 14.—Plot of the sextupole Poisson noise estimate (*horizontal axis*) vs. the magnitude of the sextupole coefficient. The galaxies falling below the straight line with slope 2.3 will be cut as having signal-to-noise ratios too small. [*See the electronic edition of the Journal for a color version of this figure.*]

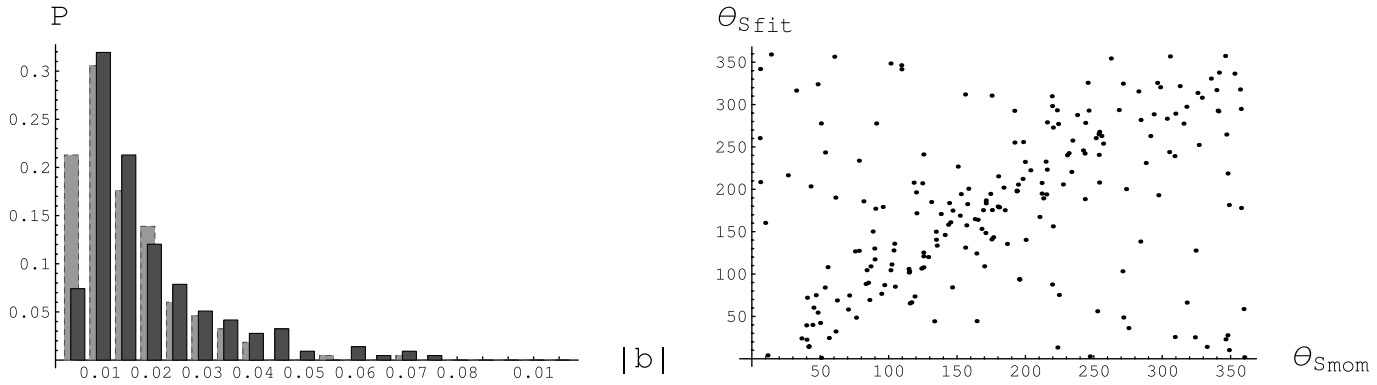

FIG. 15.—Comparison, after signal-to-noise cut, of the magnitude of the sextupole map coefficients for the moment method (*background*) and the radial-fit method (*foreground*; *left*) and of their angular orientation (*right*). The units are $(\mathrm{HDF\ pixel})^{-1}$. Multiply by 25 to get units arcsec^{-1}. [*See the electronic edition of the Journal for a color version of this figure*.]

6.5. *Fisher-Matrix-based Noise Estimates*

A standard, and perhaps more reliable, way to estimate the uncertainties in measuring the parameters of our model is to construct the Fisher information matrix. For a general review, see Tegmark et al. (1997, 1998) and references therein. See also the appendix of Kim et al. (2004) and Kallosh et al. (2003). The Fisher matrix method provides an approximation to the likelihood surface for the model parameters p_i given a set of observations x_k.

The Fisher matrix is defined by the expectation value

$$F_{ij} \equiv \left\langle -\frac{\partial^2 \ln L(\boldsymbol{x},\bar{\boldsymbol{p}})}{\partial p_i\, \partial p_j} \right\rangle = \left\langle \frac{\partial \ln L(\boldsymbol{x},\bar{\boldsymbol{p}})}{\partial p_i} \frac{\partial \ln L(\boldsymbol{x},\bar{\boldsymbol{p}})}{\partial p_j} \right\rangle, \quad (36)$$

where $L(\boldsymbol{x},\boldsymbol{p}) = \prod_{k=1}^{K} f(x_k,\boldsymbol{p})$ is the combined probability distribution and $f(x_k,\boldsymbol{p})$ is the probability distribution of the individual measurement x_k, which in general depends on the model parameters $\boldsymbol{p} = (p_1, \ldots, p_N)$. Here $\bar{\boldsymbol{p}}$ denotes the true (unknown) parameter value of $\boldsymbol{p}$. In cases when the probability distribution function L can be approximated by a Gaussian, the Fisher matrix elements can be easily calculated.

In our case the data set consists of the measurement of the number of photons and the variance for each pixel of the image. The combined probability distribution could be presented as a product of Gaussian functions for each pixel of the stamp,

$$f_{k,l}(n,\boldsymbol{p}) = \frac{1}{\sqrt{2\pi}\sigma_{k,l}} \exp\left\{ -\frac{\left[n - i_F(\boldsymbol{r}_S,\boldsymbol{p})_{k,l}\right]^2}{2\sigma_{k,l}^2} \right\}, \quad (37)$$

where $i_F(\boldsymbol{r}_S,\boldsymbol{p})_{k,l}$ is the number of photons for the (k,l) pixel according to our model, as specified by equations (21)–(23), and $\boldsymbol{p} = (A,B,C,D,x_0,y_0,a,b,d_1,d_2)$ is the set of the 14 parameters of our model (12 in the case when we set $d_1 = 2\bar{d}_2 = d$). We take the σ of the noise for the (k,l) pixel to be

$$\sigma_{k,l} = \sqrt{i_F(\boldsymbol{r}_S,\boldsymbol{p})_{k,l} + \sigma_{\mathrm{sky}}^2}, \quad (38)$$

where σ_{sky}^2 is the variance of the sky noise.[18] The combined probability distribution is $L(n,\boldsymbol{p}) = \prod_{k=1,l=1}^{\mathrm{stamp}} f_{k,l}(n,\boldsymbol{p})$.

[18] This formula is not exact due to the presence of the correlated noise between pixels due to image processing.

The Fisher matrix in this case is

$$F_{ij} = \left\langle \sum_{k=1,l=1}^{\mathrm{stamp}} \frac{\partial \ln f_{k,l}(n,\boldsymbol{p})}{\partial p_i} \frac{\partial \ln f_{k,l}(n,\boldsymbol{p})}{\partial p_j} \right\rangle = \sum_{k=1,l=1}^{\mathrm{stamp}} \frac{\partial i_F(\boldsymbol{r}_S,\boldsymbol{p})_{k,l}}{\partial p_i} \frac{\partial i_F(\boldsymbol{r}_S,\boldsymbol{p})_{k,l}}{\partial p_j} \frac{1}{\sigma_{k,l}^2} \left(1 + \frac{1}{\sigma_{k,l}^2}\right). \quad (39)$$

The Fisher matrix gives the estimate for the confidence regions for each point of the parameter space. Here we are interested only in the confidence regions for parameters (a_x, a_y, b_x, b_y) that define the confidence region for the angle δ between the quadrupole and sextupole directions. We marginalize over all other parameters.

The plot of Figure 21 shows that the estimates for variances σ_δ using equation (39) and $\sigma_{\delta\mathrm{fit}}$ using equation (34) are indeed similar.

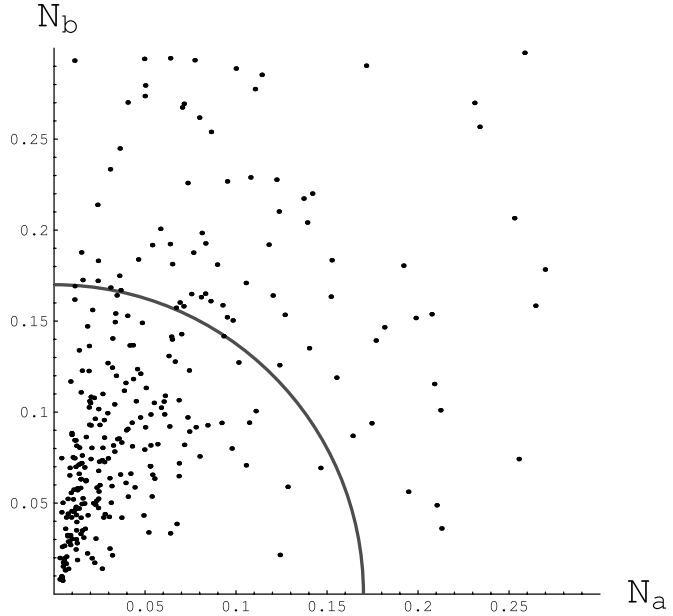

FIG. 16.—Plot of the ratio $N_a = \frac{1}{2}(\tan^{-1}|a_{xN}/a_{\mathrm{fit}}|)$ vs. the ratio $N_b = \frac{1}{3}(\tan^{-1}|b_{xN}/b_{\mathrm{fit}}|)$. The circle shows the cut condition of eq. (35). The galaxies falling outside the circle will be cut as having quadratically combined signal-to-noise ratios too small. [*See the electronic edition of the Journal for a color version of this figure*.]

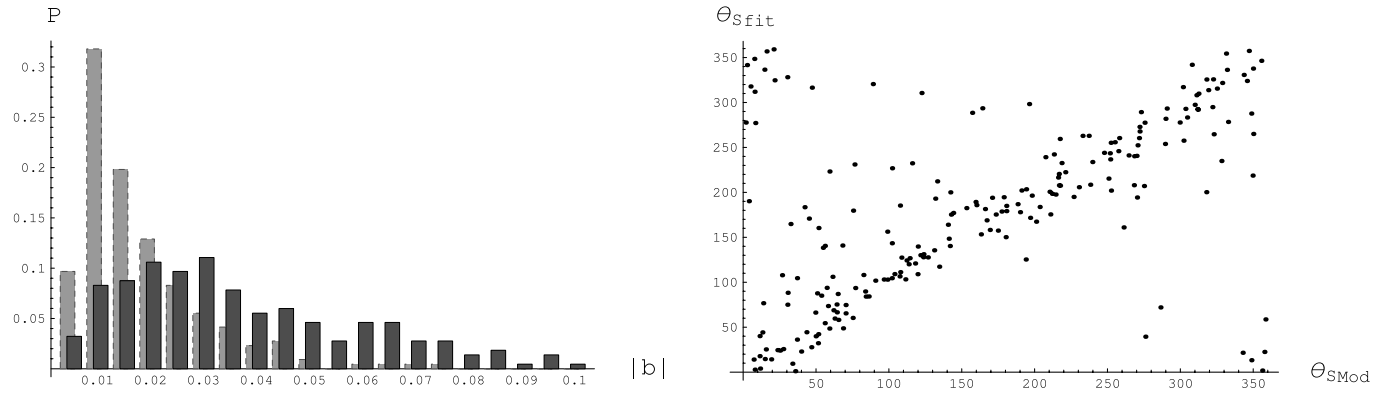

FIG. 17.—*Left:* Distribution of the magnitude of the sextupole map coefficient, for the model method (*foreground*) as compared with the radial-fit method (*background*). The units are (HDF pixel)$^{-1}$. Multiply by 25 to get units arcsec^{-1}. *Right:* Comparison of the angular orientation of the sextupole map coefficient for the model method and the radial-fit method. [*See the electronic edition of the Journal for a color version of this figure*.]

We now proceed to a study of the spatial distributions of the curved and aligned galaxies.

7. CLUMPING PROBABILITIES

To quantify clumping for a particular galaxy subset with N_S (S for subset) members, we draw a circle of fixed radius R about each member of the subset and count the members of that subset that lie within the circle. We then compare the distribution of the number of galaxies having a number of neighbors $N = 0, 1, 2, 3$, etc., within the circle, with a large number of such distributions derived from randomly chosen subsets having the same number (N_S) of galaxies in two distinct ways:

1. For an informative but qualitative comparison, we compare the distribution of the particular subset with the average distribution of the random subsets.
2. For a quantitative comparison, for the particular subset being studied and for each of 500 randomly selected subsets having the same number of galaxies as the original subset, we determine the number n of galaxies having $N \geq N'$ or more neighbors (usually $3 \leq N' \leq 7$). We then create a bar graph, showing for each value of n the fraction of the 500 random subsets that had n galaxies with N' or more neighbors. This distribution is thus a property of random subsets with N_S members, with specified neighbor distance R, for the number of neighbors $\geq N'$. Since the initial subset will have a certain number, n_0, of galaxies having N' or more neighbors, we can ask the question, what fraction of randomly chosen galaxy subsets have n_0 or more galaxies with N' or more neighbors? We thereby determine a probability that this configuration could occur by chance.

In a variation of this, the randomly chosen subsets may be constrained in some way. For example, we may wish to look only at randomly chosen subsets whose members are selected to have the same z-distribution as the galaxies in the original set.

In this section we show examples of (1) bar graphs showing the galaxy fraction (P) versus number of neighbors, for both the observed subset and for the average of 500 random subsets, whether the observed subset be aligned, midrange, or curved; (2) bar graphs showing the number of galaxies having N' or

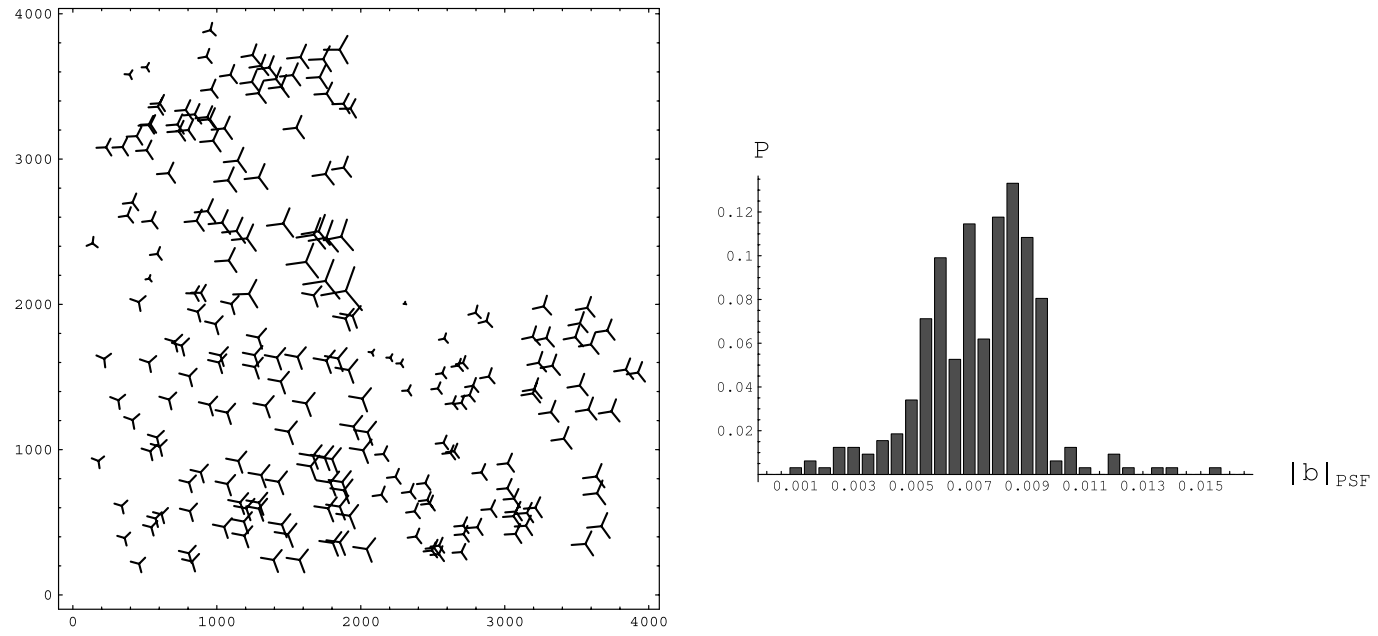

FIG. 18.—Spatial distribution of sextupole orientations (*left*) and the sextupole coefficient distribution (*right*) for the 5 times subsampled and drizzled Tiny Tim PSFs for the WFPC2 on the *HST*. The units are (HDF pixel)$^{-1}$. Multiply by 25 to get units arcsec^{-1}. [*See the electronic edition of the Journal for a color version of this figure*.]

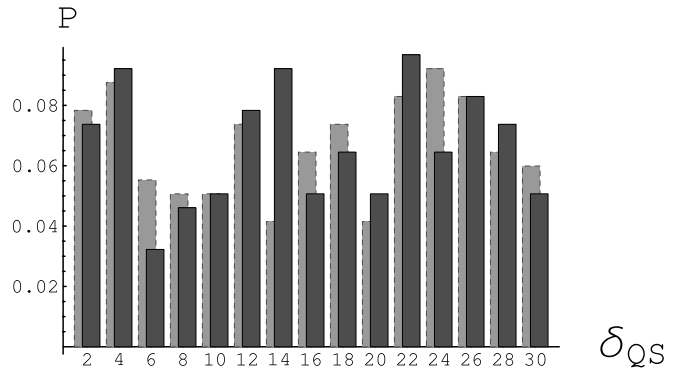

FIG. 19.—Distribution of the magnitude of δ, the smallest angle between a quadrupole minimum and a sextupole minimum, using the model method, for galaxies in the HDF-N surviving the cut condition of eq. (35) (*foreground*) and all galaxies surviving the L2 cut (*background*). [*See the electronic edition of the Journal for a color version of this figure.*]

more neighbors for 500 random subsets of the background galaxies (after cuts); and (3) field plots showing the spatial location in the field of the curved galaxies and the aligned galaxies. On these field plots we may also show the direction of the curvature of curved galaxies and/or the circular areas defining the neighborhoods of curved or aligned galaxies.

7.1. *Curved Galaxies*

We have tentatively defined curved galaxies as having $|\delta| < \delta_{\max} = 10^\circ$, but in this section we allow the precise definition to vary. The bound should not be smaller than the spread in δ from Poisson noise.[19] However, a smaller bound has the advantage of increasing the probability that the galaxy shape resulted from a lensing event. On the other hand, taking the maximum δ to be too small will decrease the number of curved galaxies and make it impossible to establish a correlation pattern.

In other words, the best definition of the curved set is not given a priori and must be sought. The optimum range, determined by iterating the considerations of this section, extends over $8\overset{\circ}{.}25 < \delta_{\max} < 9\overset{\circ}{.}25$. The results quoted here are for $\delta_{\max} = 9^\circ$.

[19] The region with $|\delta| < 10^\circ$ has an angular width of 20°.

For curved galaxies we begin with two bar graphs of type 1. In Figure 22 (*left*), using the radial-fit method, we show the distribution of neighbor counts within a circle of radius $R = 280$. In Figure 22 (*right*) we show the same distribution using the model method. Each of these distributions has an excess at larger numbers of neighbors as compared to distributions derived from averaging the same distributions for 500 randomly chosen galaxy subsets of the same size. In Figure 23 we show (for the model method) how this distribution changes as the radius of the circle is varied.[20]

Figure 24 (*left*) displays an analysis of type 2 for the radial-fit method. (The number n_0 corresponding to the curved set is indicated by an arrow.) For the optimum radius of 310 pixels, 21 of 500 random subsets have as many neighbor circles (with a neighbor count $N \geq 4$) as the curved subset. In other words, the probability of achieving the curved set by chance is about 4%. Figure 24 (*right*) displays the same analysis for the model method. The optimum radius is now 270 pixels, and the probability to achieve the curved set by chance is again 4%.

Figure 25 shows field plots of curved galaxies in the HDF-N for galaxies having three or more neighbors in neighborhood circles of radius $R = 280$ pixels. The left panel shows clumping of curved galaxies as determined using the radial-fit method. This can be compared with the right panel, the same plot with curved galaxies determined using the model method. In these plots, large stars indicate curved galaxies, and small stars indicate the remaining background galaxies. As seen in Figure 19, the change in δ is large enough that many galaxies move across the boundary defining curved galaxies. Still, the overall pattern remains remarkably similar for the two methods.

Next, for the model method, we carry through the same analysis with a less stringent noise cut. See Figure 26. Remarkably, the probability to randomly match the clumping decreases to 3% as we increase the radius of the noise cut condition of equation (35) from 0.17 to 0.25.[21] If we were truly adding noise, one would have expected the distribution to become more random,

[20] At $z = 0.6$ for current cosmological parameters (baryons 4%, dark matter 23%, and dark energy 73%), the distance scale would be 6.67 kpc arcsec^{-1}. Since the HDF images have a drizzled pixel size of $0\overset{''}{.}04$, 280 pixels corresponds to 75 kpc at $z = 0.6$.

[21] For a sense of the content of this cut change, see Fig. 16.

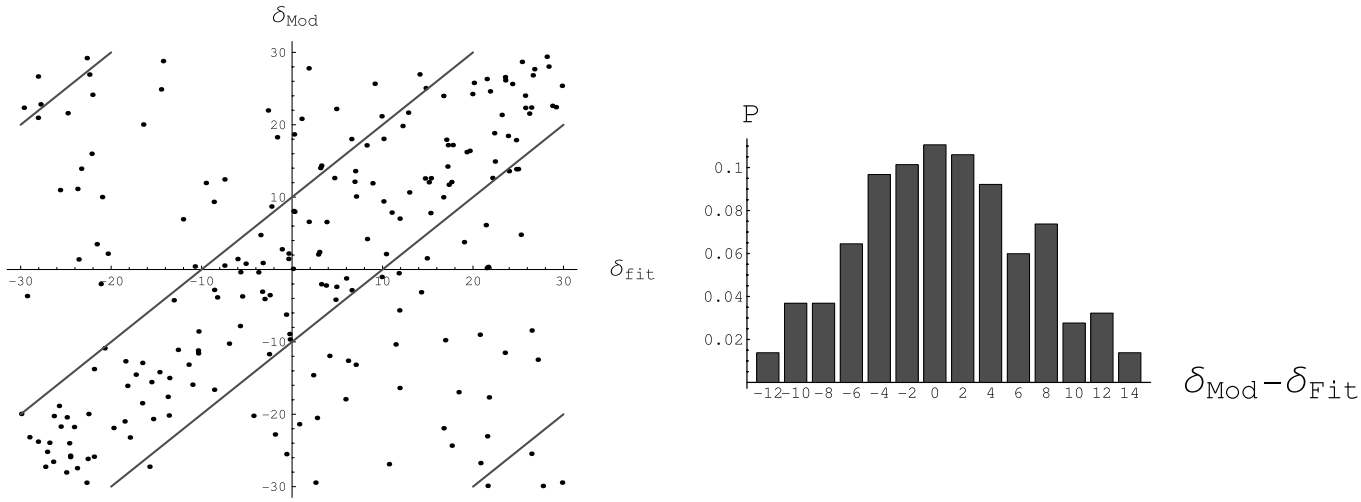

FIG. 20.—*Left:* Comparison of the angle δ as measured by the radial-fit method and the model method. The points within the diagonal band (or in the corners) have a change in $\delta < 10^\circ$. *Right:* Distribution for $\delta_{\rm mod} - \delta_{\rm fit}$. [*See the electronic edition of the Journal for a color version of this figure.*]

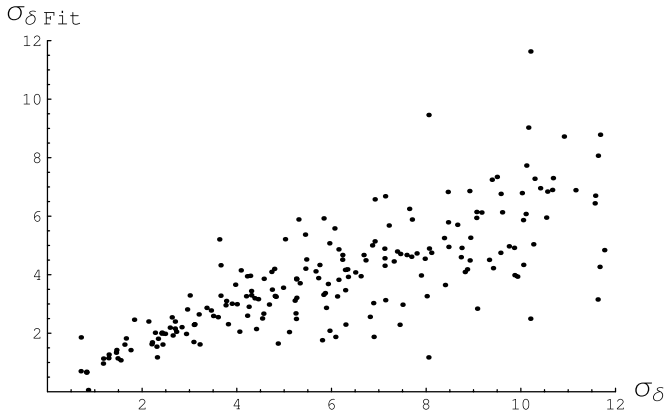

FIG. 21.—Comparison between σ_δ (in degrees) for the curvature parameter δ from the noise estimation of eq. (34) and the Fisher matrix estimations $\sigma_{\delta\mathrm{fit}}$ (eq. [39]). Values for σ_δ and $\sigma_{\delta\mathrm{fit}}$ were calculated for each galaxy fit.

not less. The new field plot is shown in Figure 26. There is now a third major clump.

Finally, we note that randomly chosen subsets often have rather improbable z-distributions. If we choose the random galaxy subsets so that their z-distributions resemble the z-distribution of the curved subset, the probability of random clumping decreases to 3%. This probability could have increased.

7.2. *Aligned Galaxies*

Since lensing by dark matter clusters will statistically move the observed shapes of background galaxies to a more curved condition (see §§ 9.1 and 9.3), the regions of the field where halos are present would be expected to have a higher number of curved galaxies, and regions of the field with a deficiency of halos would be expected to have a larger density of aligned galaxies. For this reason, one might expect aligned galaxies to also be clumped. As with § 7.1, we have carried out the following clumping considerations for several definitions of aligned galaxies, settling on $22^\circ \leq |\delta| \leq 30^\circ$.

In Figure 27 (*left*) we show an example of type 1. The distribution shows the number of aligned galaxies in a circle of radius $R = 350$ using the radial-fit method. In Figure 27 (*right*) we show the same distribution using the model method. Although the clumping is strongest at this radius, the situation does not change markedly as the radius of the circle varies from 320 to 370 pixels, for both the model method and the radial-fit method.

Figure 28 displays an analysis of type 2 for the radial-fit and model methods. Typically, for the optimum radius, between 350 and 370 pixels, there will be less than 20 out of 500 sets having as many galaxy circles with counts equal to or greater than the original curved set. In other words, the probability of achieving the aligned set by chance is equal to or smaller than 4%.

Finally, Figure 29 shows field plots for the aligned galaxies and their neighborhood circles of radius $R = 350$ pixels. The left panel is for the radial-fit method, to be compared with the right panel using the model method. In these plots, large stars indicate aligned galaxies and small stars indicate the remaining background galaxies. Shaded areas show the combined interiors of the aligned neighborhood circles.

Although the aligned set is not completely independent of the curved set (it represents half of the complement of the curved galaxies), the fact that aligned galaxies are also clumped is not a trivial consequence of the fact that curved galaxies are clumped. Indeed, galaxies midway between curved and aligned are not clumped.

7.3. *Midrange Galaxies*

Midrange galaxies behave quite differently from the curved and aligned galaxies. Figure 30 displays an analysis of type 2 for the radial-fit method (*left*) and the model method (*right*). The number n_0 corresponding to the midrange set is indicated by an arrow in this bar graph. There is no indication of clumping.

Our conclusions to this point are that the curved and aligned galaxies appear to be unusually clumped. The significance of the 4% probability must be questioned, because we have adjusted the angular range defining the curved and aligned galaxies, as well as the radius of curvature defining neighbors. On the other hand, the clumping is present for both the radial-fit and model methods. Furthermore, when the noise cut was relaxed, the probability of clumping by chance decreased to 3% without adjustment of the angular range. In addition, the probability decreases to 3% when the random sets are constrained to have the z-distribution of the original set. However, it is clear that a larger field with a comparable or larger number of background galaxies per arcminute must be analyzed to reach a convincing statistical conclusion.

8. SYSTEMATIC ERROR SOURCES

In this section we turn our attention to possible systematic nonlensing sources of the observed clumping.

8.1. *Background Galaxy Clumping*

Could the observed clumping of curved galaxies originate in the background galaxies themselves? Since the galaxies at any given slice in z are known to be spatially correlated, clumping would naturally result if the galaxies in particular galaxy groups possessed the features we are measuring. This could arise in two distinct ways: (1) There might be some age-dependent process at work. For example, perhaps old galaxies are more curved. (2) Perhaps some galaxy groups tend to be more curved than others, because of some common history or composition.

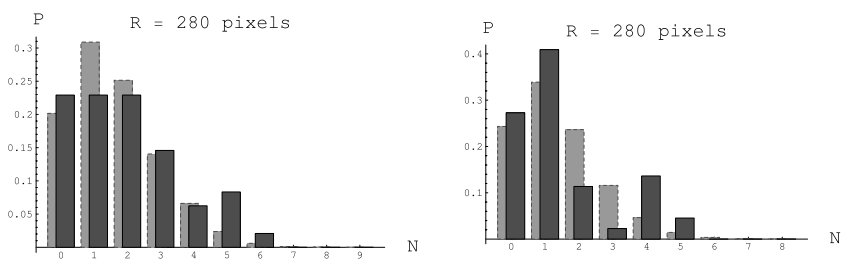

FIG. 22.—For the curved galaxy subset, for a circle radius of $R = 280$ pixels for both the radial-fit (*left*) and model (*right*) methods, histograms showing how the number of neighbors N within the circle is distributed. Those distributions are compared with the average of such distributions for 500 randomly chosen subsets having the same number of galaxies. [*See the electronic edition of the Journal for a color version of this figure.*]

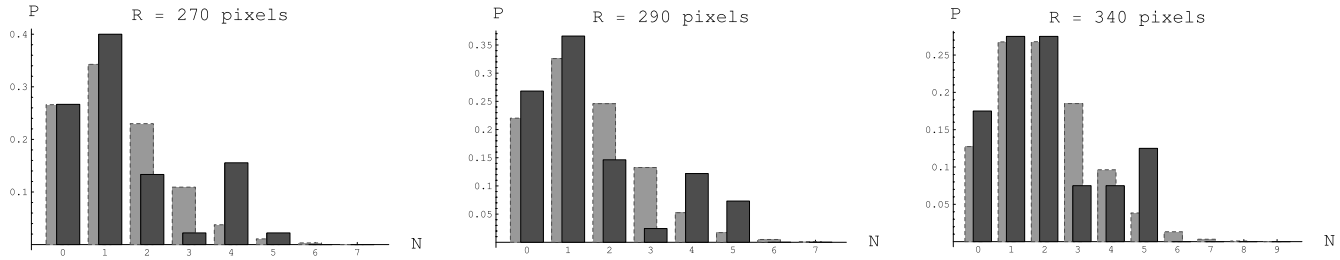

FIG. 23.—For the curved galaxy subset for the model method, three histograms for circle radii $R = 270$, 290, and 340 pixels, showing how the number of neighbors N within that circle is distributed. These distributions are compared with the average of such distributions for 500 randomly chosen subsets having the same number of galaxies. There is a suggestion of an excess in the curved subset for $N \geq 4$. [*See the electronic edition of the Journal for a color version of this figure*.]

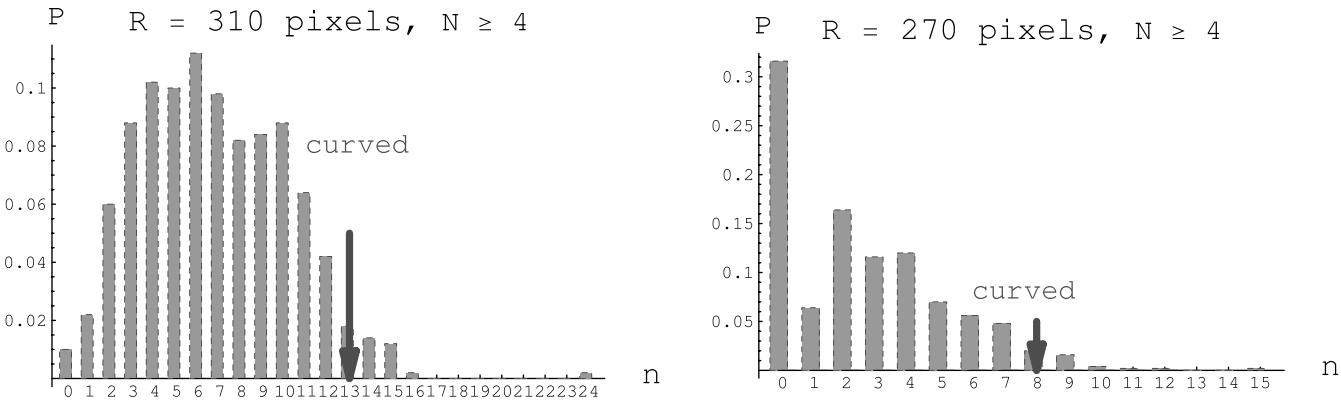

FIG. 24.—For the model method, two histograms, for circles of radius $R = 310$ and 270 pixels, showing how 500 randomly chosen galaxy subsets are distributed as a function of their number n of galaxies having four or more neighbors. The left panel is for the radial-fit method, and the right panel is for the model method. The arrow indicates the number of galaxies in the curved galaxy subset having four or more neighbors. Only a few percent of random subsets have as many or more galaxies with four or more neighbors. [*See the electronic edition of the Journal for a color version of this figure*.]

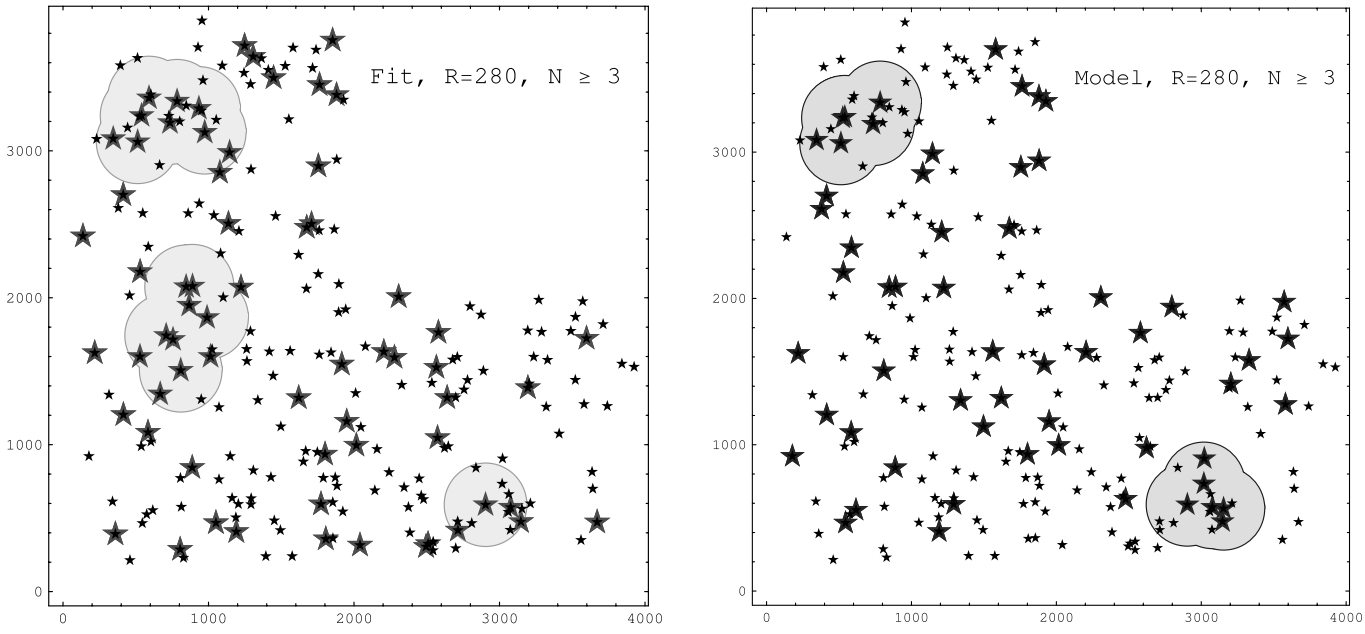

FIG. 25.—Field plot showing the spatial location of curved galaxies in the HDF-N using the radial-fit (*left*) and model (*right*) methods to determine the lensing distortion map coefficients. Large stars indicate curved galaxies, and small stars indicate the remaining background galaxies that survived the joint-variable signal-to-noise cut. Circles are shown for three or more neighbors. [*See the electronic edition of the Journal for a color version of this figure*.]

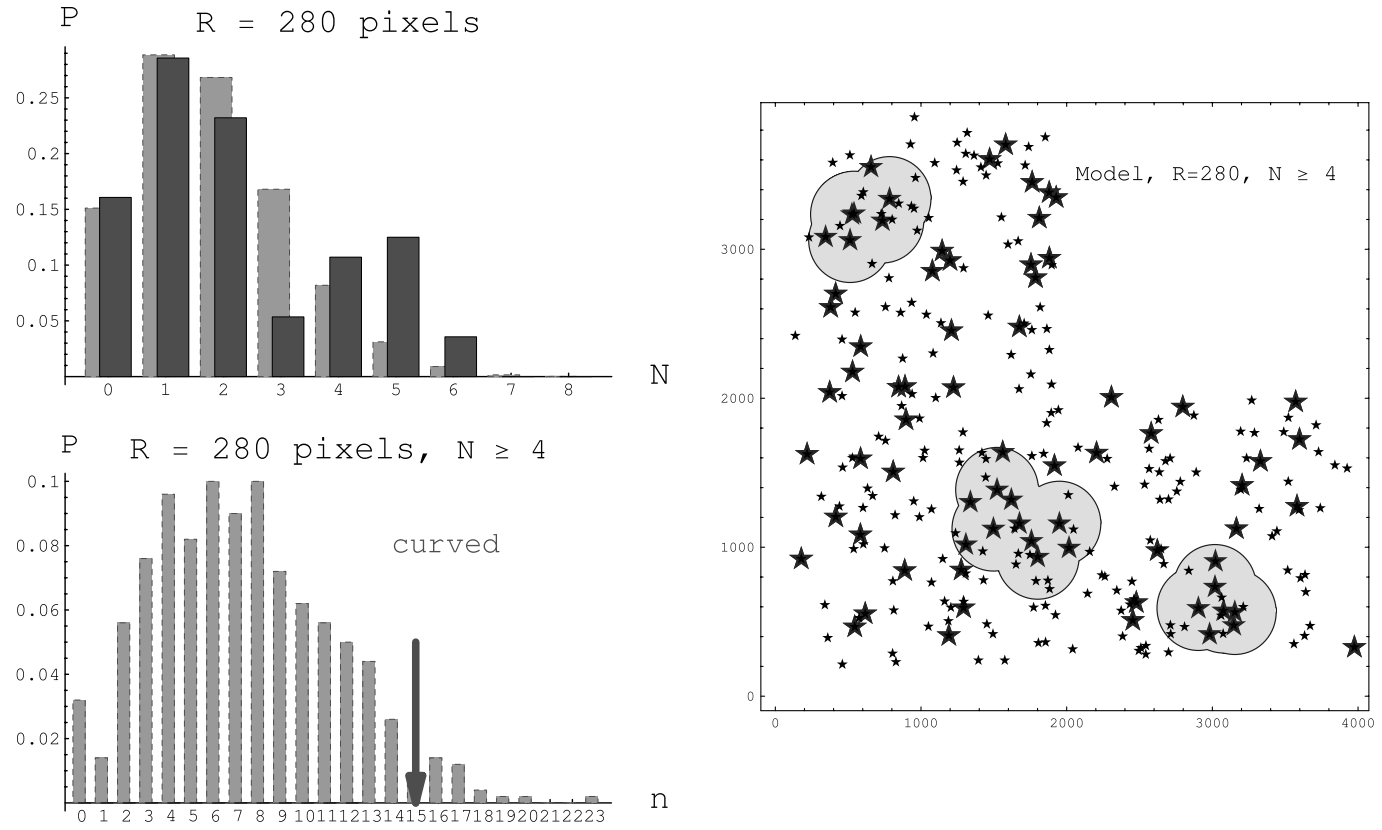

FIG. 26.—For the model method with a less stringent noise cut than Fig. 25, a neighbors histogram (*top left*), a type 2 analysis (*bottom left*), and a field plot showing the spatial location of curved galaxies in the HDF-N. Circles are shown for four or more neighbors. [*See the electronic edition of the Journal for a color version of this figure.*]

In response to item 1, one can look at the z-distribution of curved or aligned galaxies to see whether there is any evidence of a bias in the population. Figure 31 (*left*) compares the z-distribution of curved galaxies with all galaxies, and the right panel compares the z-distribution of aligned galaxies with all galaxies. There is no particular evidence that older galaxies are more or less curved or aligned, according to our criteria for curved and aligned.

To address item 2, we first note that z-values are measured in intervals of $\Delta z = 0.02$. At $z = 1.0$, 2.0, and 3.0, a separation of $\Delta z = 0.02$ corresponds to a comoving separation of 50, 30, and 20 Mpc, respectively. Therefore, galaxies in different z-bins are well separated in three-dimensional space, and an event in one group should not be able to influence another group. Hence, item 2 also appears unlikely, for three reasons:

1. None of the z-bin groups seems to be especially curved. Plotting Figure 31 for $\Delta z = 0.02$ bins shows no striking evidence that any group is particularly curved.
2. The same z-bin galaxy groups are spread across large regions of the *HST* field. Their intergalaxy separation is typically larger than the scale of the correlation we are noticing.
3. For each actual curved group we have observed, all members have distinct z-values. One can check the groups to verify that in each group there is no z-value occurring more than one time. The z-values for the upper left curved clump are $z = 1.12$,

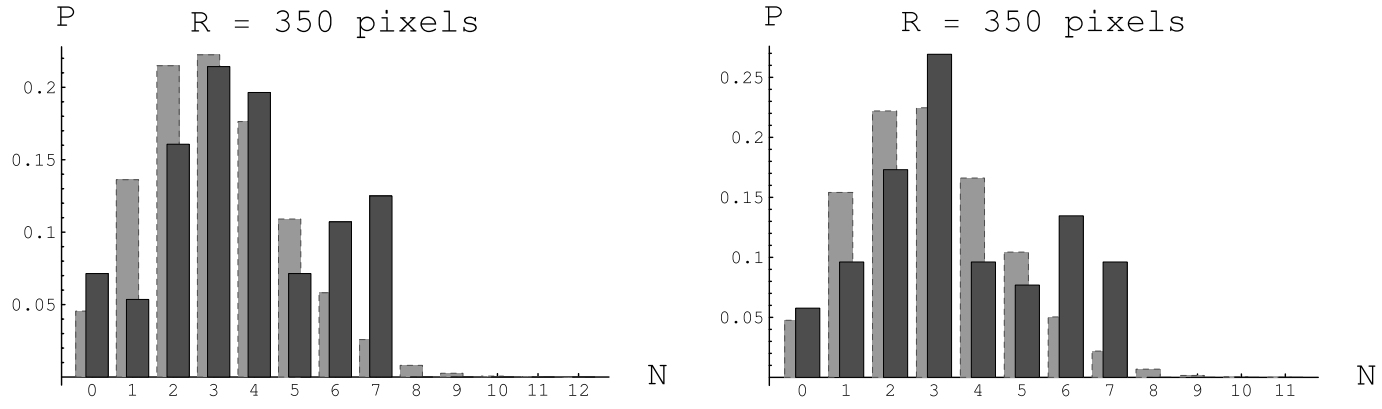

FIG. 27.—Histograms showing the distribution of the number of aligned neighbors of aligned galaxies within a circle of radius $R = 350$ pixels, compared with the average of such a distribution for 500 randomly chosen subsets of galaxies in the HDF-N having the same number of members. The left panel is for the radial-fit method, and the right panel is for the model method. [*See the electronic edition of the Journal for a color version of this figure.*]

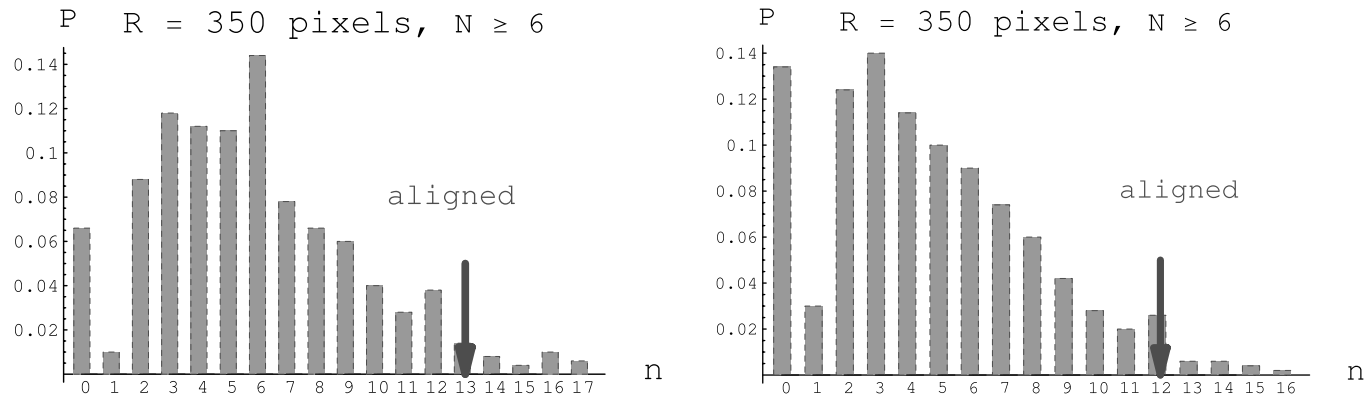

FIG. 28.—Histograms showing the fraction (P) of galaxy subsets among 500 randomly chosen galaxy subsets having n galaxies with six or more neighbors in a circle of $R = 340$ pixels. The arrow indicates the number of aligned galaxies having six or more neighbors in the aligned subset. The left panel is for the radial-fit method, and the right panel is for the model method. [*See the electronic edition of the Journal for a color version of this figure*.]

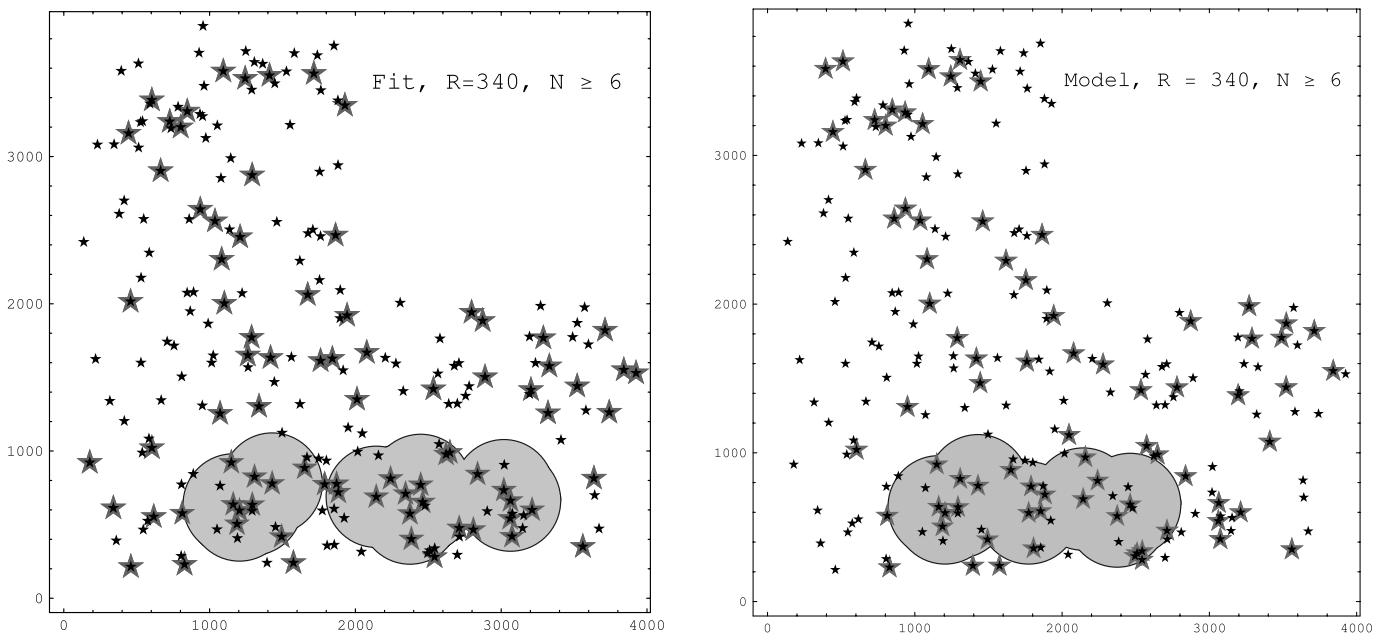

FIG. 29.—Field plots for aligned galaxies in the HDF-N field comparing the radial-fit and model methods. Neighborhood circles have a radius of 340 pixels and are required to contain four or more neighbors. The left panel used the model method, and right panel used the radial-fit method. Shaded areas show the interiors of the aligned neighborhood circles. [*See the electronic edition of the Journal for a color version of this figure*.]

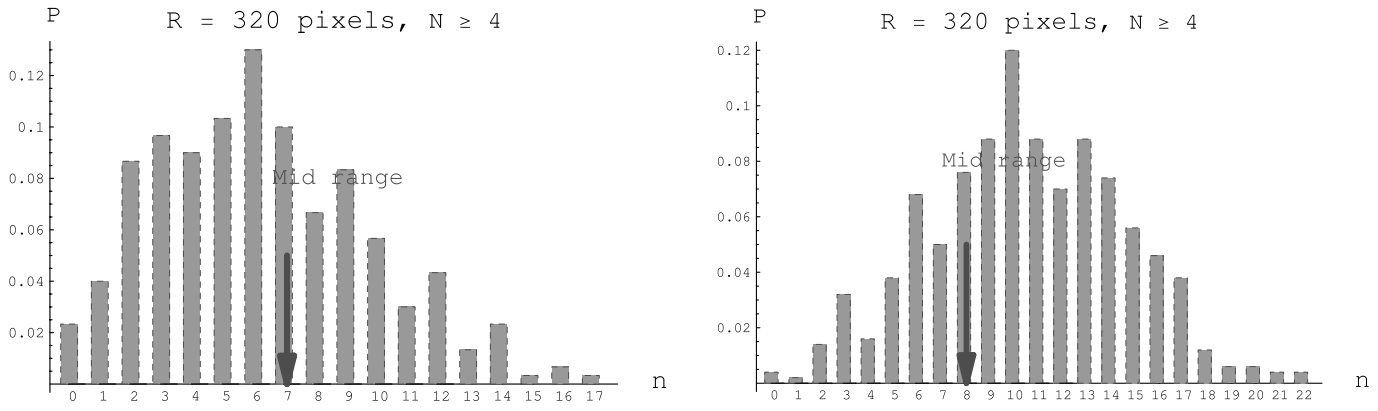

FIG. 30.—For the radial-fit (*left*) and model methods (*right*), two histograms for circles of radius $R = 320$ pixels, showing how 300 randomly chosen galaxy subsets are distributed as a function of their number n of galaxies having four or more neighbors. The arrow indicates the number of midrange galaxies with four or more neighbors. [*See the electronic edition of the Journal for a color version of this figure*.]

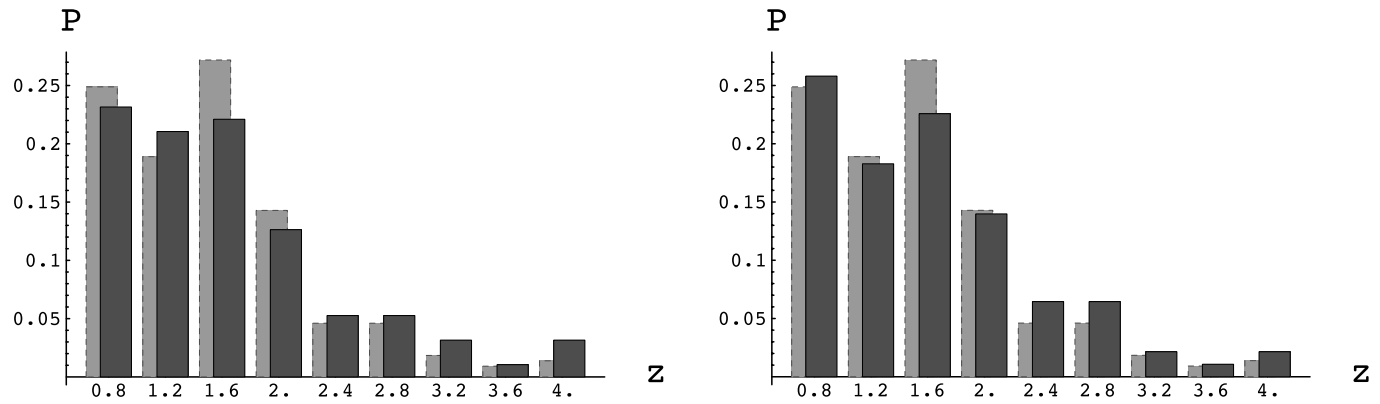

FIG. 31.—*Left:* Bar graph comparing the z-distribution of curved galaxies in the foreground bars and all galaxies in the background bars. *Right:* Bar graph comparing the z-distribution of aligned galaxies in the foreground bars and all galaxies in the background bars. [*See the electronic edition of the Journal for a color version of this figure.*]

1.16, 1.56, 1.72, 2.12, and 3.00. The z-values for the lower right curved clump are $z = 0.08$, 1.64, 1.72, 2.16, 2.24, and 3.10. Therefore, their curvature could not arise from a single causative event.

In summary, we find it to be highly unlikely that the excess clumping we are seeing for both curved and aligned galaxies could result from correlated shapes present in the background galaxies themselves.

8.2. *PSF Residuals*

We know that the PSF correction plays a role in the determination of which galaxies are curved, and we have made an effort to remove the PSF effects, but are there significant residuals? Unfortunately, the PSF can vary with time, as the temperature of the *HST* changes. However, there are reasons to doubt that the observed clumping is coming from the PSF.

Figures 12 and 18 show the orientation and magnitude of the quadrupole and sextupole coefficients for the Tiny Tim PSF, respectively. We note that the orientation of the sextupole coefficient is almost constant in each chip, and the magnitude varies only slightly. This is in strong contrast to the quadrupole moment, which gets stronger at the edges of the chips and whose orientation follows large circles, centered roughly on the chip. Combining these two would result in a pattern that would repeat six times around each circle (curved → midrange → aligned → midrange → curved → . . .). For three orientations of the quadrupole a minimum is aligned with a minimum of the sextupole, and each such orientation occurs twice, on opposite sides of the circle. The radius of this circle is ∼800 pixels, and hence the circumference is ∼4800 pixels. Each repeat has a length of ∼800 pixels, and hence the curved region width would be ∼270 pixels. In other words, these regions would have half the radius of the clumped regions we have found and one-quarter the area. No such pattern is apparent, and the regions predicted to be curved do not correspond to the locations of our clumped regions.

8.3. *Image Composition*

Since we suspect that we are processing images in a way not originally anticipated by the creators of the image composition process, we were concerned that our observations could be due to a feature of that process. We raised this concern with the Space Telescope Science Institute, who assured us that "to [our] knowledge, there are no instrument artifacts or any portion of the image processing and stacking which would mimic the curvature you are noting in the background galaxies."[22]

The final image is the co-addition and drizzling of images that were taken with nine distinctly dithered pointings, enabling the resolution of the composite image to be higher than any single image. The dither offsets have to be known accurately at each point on the focal plane, or else the co-addition will indeed yield image moments not present in the original images. But this is a question of magnitude. As we have repeatedly pointed out, the magnitude of any distortion must be of the order of the observed moments themselves. In the case of the quadrupole, suppose we have a false separation of two symmetrical images each offset by Δ but in opposite directions. Then, a false quadrupole map coefficient of magnitude $\frac{1}{2}(\Delta/r_0)^2$ will be generated. For this to have a magnitude of a typical $a \approx 0.2$ would require $\Delta/r_0 \sim 0.6$. Since our typical $r_0 \geq 3$, this would require $\Delta \geq 1.8$ HDF pixels. In our opinion, this is an improbably large offset. We would estimate false offsets to be at most 1/4 this size (0.2 original camera pixels). With the effect going as the square, that would be a factor of 16 too small. Similarly, the false sextupole generated by three images each offset in a triangular configuration by Δ would have a sextupole coefficient of magnitude $\frac{1}{6}(\Delta^3/r_0^4)$. For this to have a magnitude of 0.02 even for $r_0 = 3$ would require $\Delta \geq 2$ HDF pixels, again at least 4 times larger than expected false offsets.

If there were errors in the dither amplitudes, one would expect these errors to be coherent across the field; that is, all of the galaxies in a local region would have the same errors in the co-addition process. This would result in a spatial clumping of curvature, but all the galaxies in any given local region would appear to be curved in the same direction. This is not what we see.

We also note that the regions where curved galaxies clump do not appear to have any particular identifiable pattern, i.e., they do not appear to coincide with chip boundaries.

8.4. *Pixel-derived Effects*

Early on, we had a concern that spurious sextupole moments could be generated by the simple process of pixelating an image. To probe this, we took known typically sized bi-Gaussian distributions and, varying the centroid, dropped them onto a pixel grid. To our surprise, the falsely induced sextupole map coefficients had strengths less than 10^{-5}. Square pixel grids do give

[22] We sent the STScI (Space Telescope Science Institute) a draft of our paper (astro-ph/0308007) that used only moment methods. This reply was received from the Help Desk on 2003 September 9, call CNSHD330235.

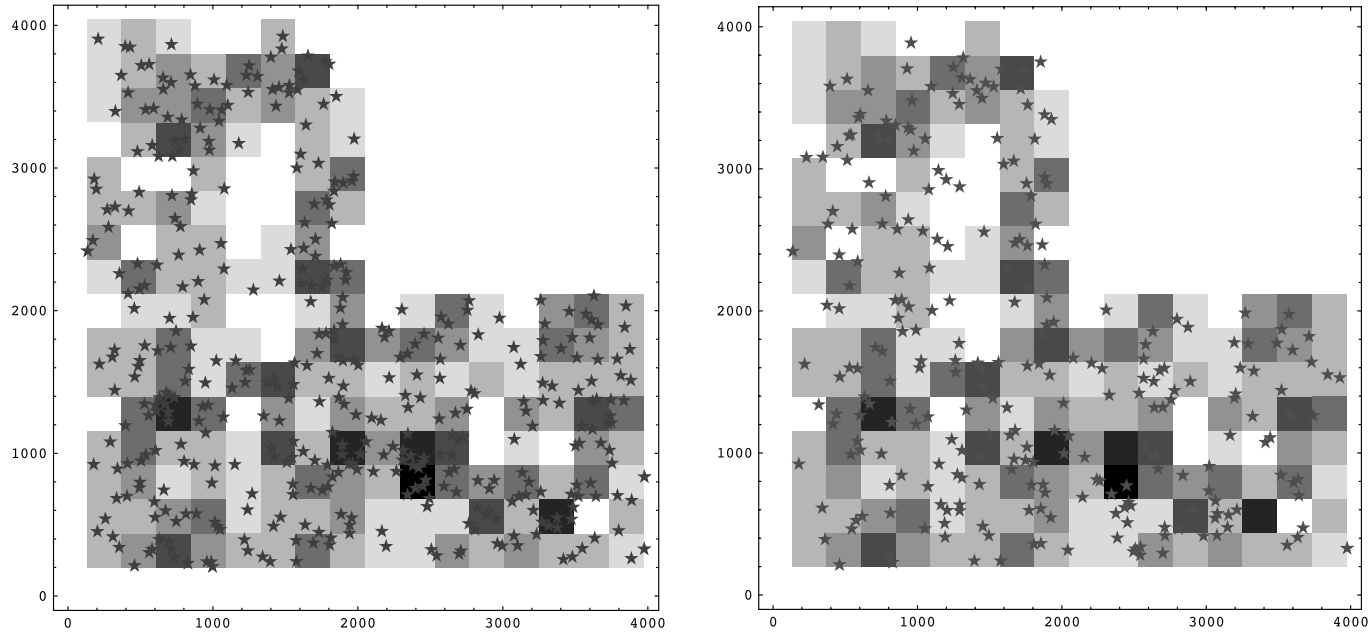

FIG. 32.—*Left:* Foreground galaxies shown as stars on a grid of 192 square boxes. The boxes are shaded according to galaxy density, with black for the most dense areas. *Right:* Same grid with the background galaxies shown as stars. Foreground and background galaxies are galaxies with $z_{\rm phot} < 1.25$ and $z_{\rm phot} > 1.25$, respectively. [*See the electronic edition of the Journal for a color version of this figure.*]

rise to spurious octupole moments, and sensitivity limits are set in that case.

Of course, pixel defects will give rise to spurious changes in galaxy shapes. Taking a hole out of one side of an image would induce a spurious curvature. Defects in the quantity and arrangement required would seem like a serious camera defect.

8.5. *Galaxy Selection Effects*

Galaxy selection software would appear to be blind to position in space and incapable of leading to the spatial clumping of curved or aligned galaxies.

9. CLUMPING IN STANDARD ΛCDM?

Are our observations of the clumping of curved and aligned galaxies consistent with what one might expect from the concordance ΛCDM model? We are not able to give a definitive answer to this question, for several reasons: (1) The HDF-N is a small field, and the statistical determination is poor. (2) There is a strong dependence of the result on the actual dark matter profiles for halos with virial mass in the range 10^{10}–$10^{13}\ M_{\odot}$. (3) Small mass halos (down to $10^{9}\ M_{\odot}$) can have an important contribution if they are strongly stripped or their mass is concentrated for any other reason. (4) A proper simulation using current ΛCDM ingredients (now in progress) must take into account the noise cuts for faint and small galaxies, the lensing mass spatial distribution, and the distribution of initial background galaxy positions and shapes, and must faithfully replicate the clumping algorithm. Nevertheless, we make some estimates and outline an approach to this question.

Our inquiry is based on the hypothesis that although the foreground galaxies are expected to be random, after positions are chosen, they will have a density pattern that can give rise to a spatial variation of curving. Indeed, in § 9.1 we exhibit the over- and underdensities of the visible foreground galaxies and find variations of apparently sufficient amplitude on spatial scales relevant to our observations.

Section 9.2 below assumes that we are dealing with a generalized Moore profile and determines the cross section of these profiles, i.e., the radius of the region (around the halo center) within which the light stream from a background galaxy would appear curved. We see a significant dependence of the cross section on the concentration and profile parameters. Section 9.3 uses the Sheth-Tormen halo distribution in conjunction with the sextupole lensing cross section determination to compute a total cross section of all halos.

A secondary purpose of this section is to indicate how sextupole lensing might be expanded to provide an interesting cosmological signal. For example, the spatial variation of aligned galaxies distinguishes regions of little or no lensing from regions having lensing. Using that fact, one can construct the change, between regions, of the distribution of galaxies in the three-dimensional parameter space described by the magnitude of the map parameters $|a|$, $|b|$, and the angle of their relative orientation. Although considerable "smearing" will occur given the range of lever arm coefficients, still the strong relationship between the strength of the quadrupole for a given sextupole, indicative of the mass of the lensing halo, may persist and permit one to draw conclusions as to the nature of the lensing masses.

9.1. *Visible Foreground Galaxy Distribution*

In Figure 32 (*left*) we plot the positions of the 420 foreground galaxies on a grid of 192 boxes. The box size is chosen to be somewhat smaller than the clumping areas (four boxes constitute the clumping circle of $R = 300$ pixels). The occupancy count for the boxes varies from 1 to 7, with a mean of 2.17 galaxies per box. Darker boxes indicate larger numbers of foreground galaxies. There are five boxes with an overdensity of 3 or more times the average density. Thus, one indeed sees a sizeable variation in foreground galaxy densities. We generated a few random distributions, and they were not too different from the observed distribution, although the observed distribution appears to have larger void areas. Foreground galaxies are those with $z_{\rm phot} < 1.25$. This separation between foreground and background is based on the geometric lever arms that enter into the lensing distortion map parameter equations. See Figure 34.

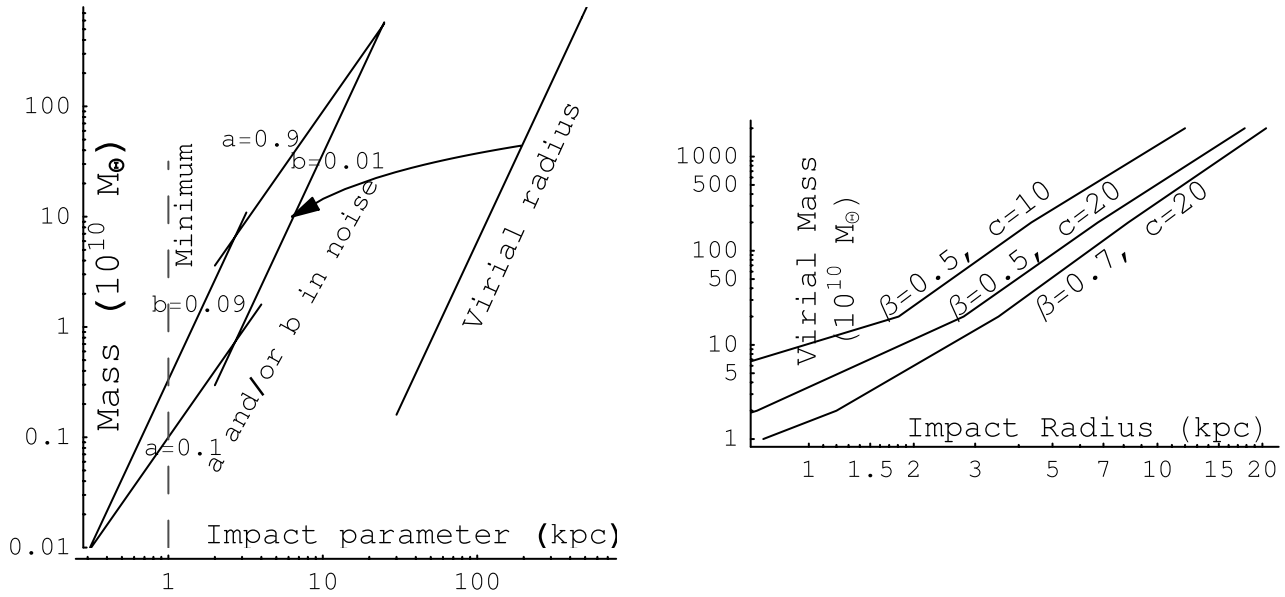

FIG. 33.—Region in (concentrated) lensing mass vs. impact radius for which a lensing mass at $z = 0.6$ would produce observable curving from sextupole lensing (*left*). Lines of constant a and b are indicated. Also indicated is the virial radius line along which dark matter halos are thought to lie. As the background galaxy trajectory probes into the interior of a halo, the enclosed mass decreases, as indicated by the curved line moving to the left from the virial radius line. However, there are terms proportional to density and its derivative that further decrease the resulting quadrupole and sextupole strengths. In the right panel, these terms are taken into account. The lines indicate the largest radii for which sextupole lensing would be observable. The lines are labeled with the β parameter ($\beta = 0.5$ is the Moore profile) and the concentration parameter c (c equals the virial radius divided by the scale radius). [*See the electronic edition of the Journal for a color version of this figure.*]

In Figure 32 (*right*) we show the background galaxies on the same grid as in the left panel. According to our conjecture, to obtain a clump of curved galaxies one would need to have (1) an overdensity of foreground halos and (2) at least nine or more background galaxies probing the overdense region. In Figure 32 (*left*) one can identify five regions with large foreground overdensities (excluding border regions). Upon checking out these regions in Figure 32 (*right*), one sees that two of those five do not have the requisite number of background galaxies probing the region. The three curved clumps of Figure 26 intersect the remaining three regions. Thus, at first glance, there would appear to be sufficient variation in foreground halo densities, and the maxima and minima are consistent with the clumping observation, although we would not want to exaggerate the importance of that conclusion.

We turn now to the particulars of lensing by dark matter halos. We would determine the conditions under which a dark matter halo produces an observable curvature.

9.2. *Sextupole Lensing Cross Sections of Dark Matter Halos*

In § 3.4 we proved that the coefficients describing the shape of the background galaxies add vectorially with the lensing-induced coefficients. This means that in order to align the orientation of the quadrupole and sextupole moments, the magnitude of lensing-induced coefficients must be competitive with the magnitude of background values. Hence, the magnitudes of a and b must be comparable with or larger than the minimum observed background values. This simple fact creates limits on the range of acceptable lensing mass and impact parameters.

Figure 33 (*left*) is a log-log plot of mass M versus impact parameter r_0 for point-mass halos. Assuming a typical lensing plane located on a plane at $z = 0.6$, with $D_{LT} = D_{LS}$ as the comoving distance to the background galaxy, one can plot loci of constant $|a|$ and $|b|$. These are straight lines with slopes of 2 and 3, respectively. Quadrupole coefficients less than 0.1 or sextupole coefficients less than 0.01 would be smaller than the background values observed, and hence such lensing would be unable to realign the intrinsic background shapes. Thus, the region to the right of these boundaries is indicated as "in the noise."

In addition, impact parameters smaller than about 1 kpc are excluded because the radii of the background-galaxy light-path footprints are at least 2.5 pixels, which is about 0.7 kpc on the $z = 0.6$ plane.

According to the concordance model, the outer radius of dark matter halos, referred to as the virial radius, r_V, depends on the total (virial) mass as $r_V \propto M_V^{1/3}$. The constant of proportionality is established by taking $r_V = 300$ kpc for $M_V = 1.6 \times 10^{12}\ M_\odot$. The locus of these "complete" dark matter halos is also designated in Figure 33 (*left*). Clearly, the a and b induced for a light stream passing at the virial radius are too small to be observable.

However, these halo radii are large (a 300 kpc = 1120 pixel radius object would fill a WFPC chip), and hence light streams certainly traverse (many) halo interiors. Using a standard NFW profile one can integrate out the variable perpendicular to the lensing plane to determine the surface mass density on the lensing plane, and from this use the formulae of equation (11) to calculate the induced a and b within the interior of the mass distribution. The trajectory of "enclosed" mass versus impact parameter is suggested in Figure 33 (*left*), but the situation is more complicated, since a and b depend not only on the enclosed mass but also importantly on Σ and Σ'. The radii at which the lensing-induced values of $a \geq 0.1$ and $b \geq 0.01$ become observable are indicated as a function of virial mass in Figure 33 (*right*). These radii depend strongly on the particulars of the halo profile. The maximum radius as a function of virial mass is shown for three profiles with concentrations (the virial radius divided by the scale radius) of 10 or 20 and density profile parameters $\beta = 0.5$ (the Moore profile) or $\beta = 0.7$, where $\rho(r) \sim r^{-1-\beta}(r+1)^{-2+\beta}$.

We see that the cores of dark matter halos are indeed dense enough to cause observable sextupole lensing for a range of halo mass extending from about $10^{10}\ M_\odot$ upward.

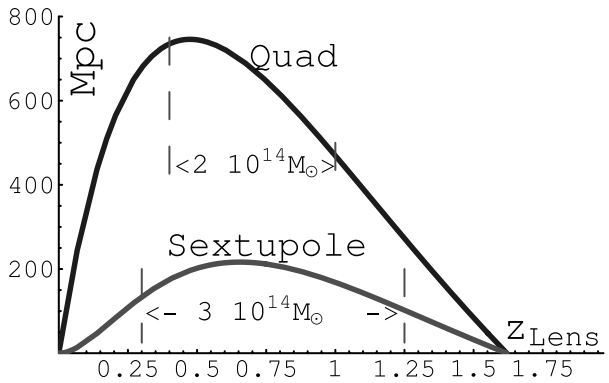

FIG. 34.—Plot of the lever arm coefficients as a function of the position of the lensing plane for the quadrupole and sextupole map coefficients for the median $z = 1.64$ background galaxy. These coefficients are given by $D_{LS}\{D_{TL}/[(1 + z_L)D_{TS}]\}$ and $D_{LS}\{D_{TL}/[(1 + z_L)D_{TS}]\}^2$, respectively. The original mass residing in the regions of large lever arm coefficients is indicated. [*See the electronic edition of the Journal for a color version of this figure.*]

9.3. *Total Sextupole Lensing Cross Section*

In Figure 34 we have plotted the geometric lever arm coefficients (the product of the D values in eq. [9]) for the quadrupole and sextupole map coefficients for a "median" $z = 1.64$ background galaxy. The geometric coefficients are large for the range $0.3 < z < 1.25$, and hence dark matter halos in this z-region could give rise to lensing. We refer to this region as the foreground. The comoving volume of the Hubble Deep Field is a needle-like truncated pyramid, having an angular width of 0.75 mrad (160″). The comoving distance to $z = 1.25$ is 3.9 Gpc, and that to $z = 0.3$ is 1.2 Gpc. The comoving volume "behind" the three WFPC chips between $z = 0.3$ and $z = 1.25$ is about 8000 Mpc^3. Using a matter density of 0.27 times the critical density ($3.7 \times 10^{10}\ M_\odot$ Mpc^{-3}) would imply that this volume originally contained a matter mass of $3 \times 10^{14}\ M_\odot$.

To estimate the number of halos within this volume, one can use the Sheth-Tormen distribution (Sheth & Tormen 1999), which is supported by N-body simulations (Reed et al. 2005). The result is that 40% of the total halo mass, $1.2 \times 10^{14}\ M_\odot$, lies in the mass range between 7×10^9 and $2.3 \times 10^{13}\ M_\odot$.

Breaking down $1.2 \times 10^{14}\ M_\odot$ by decade, eight halos totaling 40% of the mass lie in the top decade above 2.3×10^{12}, 61 halos representing 30% of the mass lie in the decade above 2.3×10^{11}, 465 halos representing 23% of the mass lie in the decade above 2.3×10^{10}, and 870 halos representing 7% of the mass lie between there and 7×10^9. There are 420 visible galaxies in the HDF-N foreground, suggesting that halos down to about 3.5×10^{10} are visible.

To define a total cross section for sextupole lensing, we have integrated the cross section times the halo density function. Since the cross section is given in kiloparsecs, there are different numbers of pixels in the cross sections for different lensing planes. Hence, it is necessary to integrate over the volume of the foreground. The relevant equation is

$$\int \pi r_{SL}(M)^2 \frac{dn}{dM}\, dM \int \left(\frac{1 + z_L}{D_{TL}\theta_p}\right)^2 3(\theta_C D_{TL})^2\, dD_{TL}, \quad (40)$$

where $r_{SL}(M)$ is the maximum sextupole lensing radius for a halo of mass M in units of Mpc, dn/dM is the halo density function (halos per unit mass per Mpc^3), $(1 + z_L)/D_{TL}\theta_p$ is the conversion from Mpc to pixels, and the rest of the expression is the volume interval for three chips, each subtending an angle θ_C.

The integral over dD_{TL} can be carried out by using the expression $dD_{TL}/dz = (c/H_0)/[0.27(1 + z)^3 + 0.73]^{1/2}$ and integrating over z, where c is the speed of light and H_0 is the Hubble constant at $z = 0$. The expression $3(\theta_C/\theta_p)^2$ is the number of pixels in the field and can be divided out to give the fractional cross section. For simplicity, we use a straight line fit to the Sheth-Tormen distribution $dn/d\log M = 1.2 \times 10^8/(M/h^{-1})^{0.88}$ Mpc^{-3} and a straight line fit to the function $r_{SL}(M)$ for $\beta = 0.5$ and $c = 20$. The mass integral is carried out from 10^{10} to $10^{13}\ M_\odot$. One finds that this estimate gives a fractional sextupole cross section equal to 4% of the field.

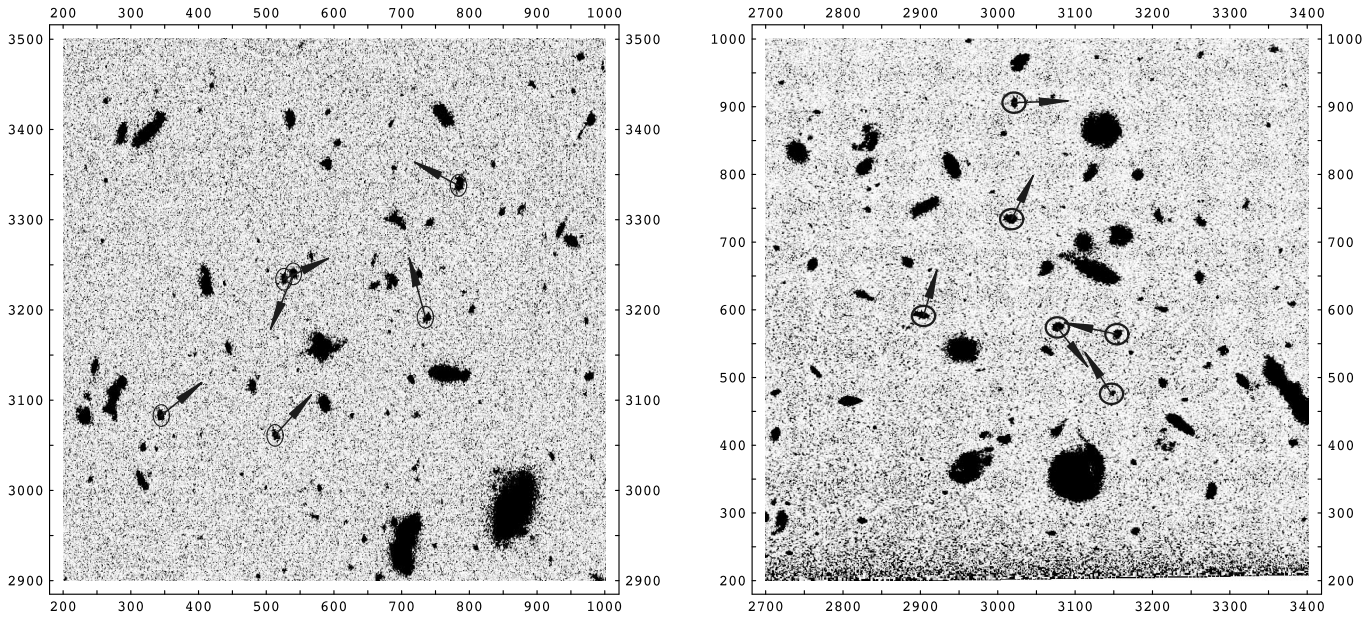

FIG. 35.—Close-up look showing all galaxies in the two regions of clumping of curved galaxies for the model method. The base of the arrow is at a curved galaxy, and the arrow points toward its center of curvature. The tick numbers indicate the pixel coordinates in the field. [*See the electronic edition of the Journal for a color version of this figure.*]

This total fractional cross section can be roughly interpreted as indicating that 1 in 25 background galaxies will experience a strong sextupole lensing event. Of course, we have made many approximations and ignored many details, so we do not want to draw any conclusions from this result other than to say that within a factor of 2 this is in the range that could reasonably explain the clumping effects we are seeing. Only a detailed simulation could provide a more accurate answer, and even that will be subject to the unknowns mentioned in the introduction to this section.

If visible halos were responsible for the enhanced clumping of curved galaxies we have observed, one would expect to see (e.g., for the model method) that, for at least one of the two curved clumps, at least two of the curved galaxies are oriented so that their curvature vectors point toward a foreground galaxy responsible for the lensing. Figure 35 shows a close-up of the two clumps identified in Figure 25. In the upper left field shown in the left panel there is one clear example of lensing and a potential second case. In the lower left of the field there is no obvious case. We take this to be inconclusive, especially since invisible halos can play a role.

10. SUMMARY

We have argued that close-encounter lensing events can produce a second-order deformation having three maxima and minima, which we refer to as a sextupole deformation. Furthermore, lensing kinematics requires that this sextupole deformation be oriented with respect to the well-known elliptical (or quadrupole) deformation (having two maxima and two minima), so that one of the two quadrupole minima is aligned with one of the three sextupole minima. Galaxies having their sextupole deformation so aligned with their quadrupole deformation are called "curved."

We have proposed that if some fraction of curved galaxies are indeed the result of a lensing event, and since the suspected lensing events are the result of a close encounter with a foreground dark matter halo, and since foreground halos are observed to be clustered on the sky, it may be true that the curved galaxies are also clustered. Thus, one should look for clustering of curved galaxies, because if clustering is observed and other less esoteric reasons for the clustering can be ruled out, one would have an indicator of the presence of close-encounter sextupole lensing.

To build a basic structure for nonlinear lensing, the concept of a "lensing distortion map" was introduced. The lensing distortion map contains the full content of the lensing event(s) and the geometry. In addition to the usual two parameters of linear lensing (convergence and shear), there are three complex second-order terms in the general map. The parameters of the map are given for lensing by an azimuthally symmetric dark matter halo.

Next we described a method to determine lensing map coefficients from the analysis of galaxy shapes. In addition to the moment methods, we have described a radial-fit method and a model method. The core of these methods is to find the best azimuthally symmetric (radial) fit to the galaxy and then to act on that radial profile with a map, adjusting parameters to find the best fit to the galaxy. In the case of the model method, application of the PSF, camera charge diffusion, and image processing procedures (drizzle) are also included in the fit process. Using these techniques, fit parameters are found for the background galaxies in the Hubble Deep Field–North.

If a galaxy has not been lensed, one can proceed in the same way and obtain a "source" map. The maps obtained for a lensed galaxy are a concatenation of a source map with a lensing map. The map coefficients obtained in the concatenation are shown to be approximately given by the linear combination of source map and lensing map coefficients.

We divided all galaxies into three groups according to the orientation of the sextupole with respect to the quadrupole distortions: curved, midrange, and aligned. Then each of these three groups was studied to determine whether they are clumped on the sky in some abnormal way or their arrangement could just as easily be a random arrangement of galaxy shapes. We have determined that the curved and aligned galaxies do not appear to be random, with the probability to be random equal to or less than 4%.

We discuss systematic effects that could give rise to an apparent clumping. The most obvious systematic effects are a property of the PSF or a property of the source galaxies themselves. We argue that these appear to be unlikely sources of clumping. For example, in the clumped groups, no two background galaxies have the same value of z, and the spatial scale on which the quadrupole and sextupole moments of the Tiny Tim PSF are varying is considerably larger than the clumping scale observed.

Finally, we discussed one scenario that could give rise to a real clumping of sextupole lensing: a nonuniform arrangement of foreground dark matter halos. We look at foreground galaxies and find that they are not uniform, of course. Then we define the concept of a sextupole lensing cross section and calculate it as a function of total mass for a Moore profile for concentration parameters of 10 and 20. The cross section depends on the location of the lensing plane and source plane. Ignoring this dependence, one can calculate an estimate for the cross section for the foreground field populated according to a Sheth-Tormen halo distribution function. Although the results are incapable of proving or disproving the hypothetical scenario, the range is within a factor of 2 of what one might have imagined was necessary. In addition, the hypothetical scenario suggests more general situations that could give rise to a sextupole lensing signal.

The Hubble Deep Field–North has an area of about 5 arcmin^2, of which only 3.3 arcmin^2 is available once a border region equal to the typical radius of neighbor circles is subtracted. In comparison, the Ultra Deep Field (UDF) has a usable area of 8.6 arcmin^2. In addition, the UDF total exposure time at the principal filter is 3 times greater, and the *HST* ACS (Advanced Camera for Surveys) used for the UDF has twice the resolution of the WFPC. Hence, we believe the UDF will provide a strong test of our methods.

Another space-based project in the planning stages (the *Supernova/Acceleration Probe*, *SNAP*; Aldering et al. 2002; Rhodes et al. 2004; Massey et al. 2004; Refregier et al. 2004) has a weak lensing program of $\sim$1000 deg^2 (10^6 times the Hubble Deep Field) with comparable resolution, better characterization of the PSF, and enough depth to provide $\sim$100 background galaxy images per square arcminute.[23]

We would like to acknowledge the encouragement and support of Tony Tyson and David Wittman of Bell Labs. Visits by both of us to Bell Labs prepared us for this undertaking, especially by introducing us to existing software and weak-lensing techniques. We would also like to thank Pisin Chen and Ron Ruth at SLAC (Stanford Linear Accelerator Center) for trusting in our judgment and encouraging us to proceed. This work was supported by DOE grant DE-AC03-76SF00515.

After presenting our ideas to Tony Tyson in 2002 January, he suggested that we look at a posting by D. M. Goldberg and P. Natarajan titled "The Galaxy Octupole Moment as a Probe of Weak-Lensing Shear Fields" (Goldberg & Natarajan 2002). The

[23] See also http://snap.lbl.gov.

mathematical formulae presented there were actually what we have been calling the sextupole. Our nomenclature derives from beam physics, where the sextupole field is created by a magnet with six poles, three of positive polarity and three of negative polarity. In addition, the lensing-induced shape has three maxima and three minima. To our knowledge, there was no mention by Goldberg and Natarajan of the induced sextupole (their octupole) shape or of using its correlation with the quadrupole shape to distinguish galaxies.

We thank Ken Shen for his assistance in providing a program to identify double-maximum galaxies and Konstantin Shmakov for help with software.

The first version of this present work was posted in 2003 August (Irwin & Shmakova 2003).

REFERENCES

Aldering, G., et al. 2002, Proc. SPIE, 4835, 146
Bacon, D. J., Goldberg, D. M., Rowe, B. T. P., & Taylor, A. N. 2006, MNRAS, 365, 414
Bartelmann, M., & Schneider, P. 2001, Phys. Rep., 340, 291
Bertin, E., & Arnouts, S. 1996, A&AS, 117, 393
Brainerd, T. G., Blandford, R. D., & Smail, I. 1996, ApJ, 466, 623
Goldberg, D. M., & Bacon, D. J. 2005, ApJ, 619, 741
Goldberg, D. M., & Natarajan, P. 2002, ApJ, 564, 65
Hoekstra, H. 2004, MNRAS, 347, 1337
Hoekstra, H., Yee, H. K. C., & Gladders, M. D. 2002a, NewA Rev., 46, 767
Hoekstra, H., Yee, H. K. C., Gladders, M. D., Barrientos, L. F., Hall, P. B., & Infante, L. 2002b, ApJ, 572, 55
Huterer, D. 2002, Phys. Rev. D, 65, 063001
Huterer, D., & Turner, M. S. 2001, Phys. Rev. D, 64, 123527
Irwin, J., & Shmakova, M. 2003, preprint (astro-ph/0308007)
———. 2004, in Quantum Aspects of Beam Physics, ed. P. Chen & K. Reil (Singapore: World Scientific), 263
Kaiser, N., Wilson, G., & Luppino, G. A. 2000, ApJ, submitted (astro-ph/0003338)
Kallosh, R., Kratochvil, J., Linde, A., Linder, E. V., & Shmakova, M. 2003, J. Cosmol. Astropart. Phys., 10, 015
Kallosh, R., & Linde, A. 2003, J. Cosmol. Astropart. Phys., 0302, 002
Kim, A. G., Linder, E. V., Miquel, R., & Mostek, N. 2004, MNRAS, 347, 909
Kuijken, K. 1999, A&A, 352, 355
Linde, A. 2004, in Science and Ultimate Reality, ed. J. D. Barrow, P. C. W. Davies, & C. L. Harper, Jr. (Cambridge: Cambridge Univ. Press), 426
Linder, E. V., & Jenkins, A. 2003, MNRAS, 346, 573
Massey, R., et al. 2004, AJ, 127, 3089
Mellier, Y. 1999, ARA&A, 37, 127
Mellier, Y., van Waerbeke, L., Bertin, E., Tereno, I., & Bernardeau, F. 2002, Proc. SPIE, 4847, 112
Moore, B. 1994, Nature, 370, 629
Moore, B., Ghigna, S., Governato, F., Lake, G., Quinn, T., Stadel, J., & Tozzi, P. 1999, ApJ, 524, L19
Moore, B., Governato, F., Quinn, T., Stadel, J., & Lake, G. 1998, ApJ, 499, L5
Natarajan, P., & Refregier, A. 2000, ApJ, 538, L113
Navarro, J. F., Frenk, C. S., & White, S. D. M. 1995, MNRAS, 275, 720
———. 1996, ApJ, 462, 563
———. 1997, ApJ, 490, 493
Peebles, P. J. 1993, Principles Of Physical Cosmology (Princeton: Princeton Univ. Press)
Reed, D., et al. 2005, MNRAS, 357, 82
Refregier, A., et al. 2004, AJ, 127, 3102
Rhodes, J., et al. 2004, Astropart. Phys., 20, 377
Schneider, P. 2006, in Gravitational Lensing: Strong, Weak, and Micro, ed. G. Meylan, P. Jetzer, & P. North (Berlin: Springer), 273
Sheth, R. K., & Tormen, G. 1999, MNRAS, 308, 119
Tegmark, M., Eisenstein, D. J., Hu, W., & Kron, R. G. 1998, ApJ, submitted (astro-ph/9805117)
Tegmark, M., Taylor, A., & Heavens, A. 1997, ApJ, 480, 22
Wittman, D. M., Tyson, J. A., Kirkman, D., Dell'Antonio, I., & Bernstein, G. 2000, Nature, 405, 143